

A Cartesian Parametrization for the Numerical Analysis of Material Instability

Journal:	<i>International Journal for Numerical Methods in Engineering</i>
Manuscript ID	Draft
Wiley - Manuscript type:	Research Article
Date Submitted by the Author:	n/a
Complete List of Authors:	Mota, Alejandro; Sandia National Laboratories, Mechanics of Materials Chen, Qiushi; Clemson University, Civil Engineering Foulk, James; Sandia National Laboratories, Mechanics of Materials Ostien, Jakob; Sandia National Laboratories, Mechanics of Materials Lai, Zhengshou; Clemson University, Civil Engineering
Keywords:	Material stability, Constitutive equations, Newton methods, Variational methods

SCHOLARONE™
Manuscripts

A Cartesian Parametrization for the Numerical Analysis of Material Instability

Alejandro Mota¹, Qiushi Chen^{2*},
James W. Foulk III¹, Jakob T. Ostien¹, Zhengshou Lai²

¹Mechanics of Materials Department
Sandia National Laboratories
Livermore CA 94550, USA

²Glenn Department of Civil Engineering
Clemson University
Clemson, SC 29631, USA

Abstract

We examine four parametrizations of the unit sphere in the context of material stability analysis by means of the singularity of the acoustic tensor. We then propose a Cartesian parametrization for vectors that lie a cube of side length two and use these vectors in lieu of unit normals to test for the loss of the ellipticity condition. This parametrization is then used to construct a tensor akin to the acoustic tensor. It is shown that both of these tensors become singular at the same time and in the same planes in the presence of a material instability. The performance of the Cartesian parametrization is compared against the other parametrizations, with the results of these comparisons showing that in general the Cartesian parametrization is more robust and more numerically efficient than the others.

Keywords: Material stability; Constitutive equations; Newton methods; Variational methods

*Email: qiushi@clemson.edu

14 1 Introduction

15 The numerical analysis of material instability plays an important role in the understanding
16 and simulation of material failure in solid mechanics problems. A reliable and efficient
17 method to determine the onset of material instability and the bifurcation directions is re-
18 quired whether one is interested in studying the instability itself or in devising numerical
19 methods to regularize the solution at the onset of the instability [1–7].

20 Herein we adopt the classical definition of material instability as the loss of the *strong*
21 *ellipticity condition*. This is equivalent to the loss of the *strong Legendre-Hadamard condition*
22 for stored energy densities that are twice continuously differentiable [8]. Loss of ellipticity
23 has also been associated with the discontinuous acceleration of propagating waves by Hill
24 [9]. We use the term *acoustic* tensor for the second-order tensor associated with the strong
25 ellipticity condition which is also known as the *localization* tensor. Although this latter
26 denomination may be more accurate, throughout this work we use the former for historical
27 reasons.

28 The determination of the loss of the strong ellipticity condition for a very general class
29 of materials can be achieved by recourse to incremental variational constitutive updates.
30 Within this framework, an incremental stress potential embodies the constitutive behavior of
31 the material during a time increment, including elasticity, viscoelasticity, viscoplasticity, and
32 rate dependence [10–16]. By using incremental variational constitutive updates, the stress
33 and the tangent moduli can be derived from a hyperelastic-like potential for constitutive
34 behavior that may include viscosity and rate dependence. This in turn provides the means
35 to apply the tools developed herein for complex inelastic materials.

36 1.1 Previous Work

37 Extensive work has been done on the subject of material instabilities. The basic theoretical
38 principles follow from the seminal work of Hadamard [17] on elastic stability and were later
39 extended to the inelastic regime by Thomas [18], Hill [9] and others. The work of Rudnicki
40 and Rice [19] and Rice [20], among others, tied the instability in the constitutive description
41 of homogeneous deformation to the onset of localized deformation, which was linked to the
42 loss of the positive definiteness of the acoustic tensor of the material at a given state. See
43 also Armero and Garikipati [4] and Miehe, Lambrecht, and Gürses [12] for a brief historical
44 overview of the development of classical localization analysis.

45 In the context of finite element analysis, existing approaches to detect material insta-
46 bility as well as the bifurcation directions generally fall into two categories: analytical and
47 numerical.

48 For certain material models under specific loading conditions, analytical solutions of
49 the instability problem can be derived. For instance, Schreyer and Neilsen [21] derived an
50 analytical criterion for the loss of ellipticity for a general class of symmetric constitutive
51 equations. Becker [22] used the Gurson constitutive model in combination with a failure
52 criterion based on material stability and bifurcation in a finite element model to predict
53 fracture and fragmentation in a dynamic expanding ring experiment. Oliver and Huespe [23]

54 provided closed-form solutions for the detection of the singularity of the acoustic tensor for
55 a wide class of small deformation isotropic and anisotropic damage models. On the basis
56 of the general Hadamard instability criterion, Xue and Belytschko [24] derived a closed-
57 form expression to determine the onset of instability and the bifurcation directions for a
58 particular damage plasticity model. These analytical approaches are computationally very
59 efficient, robust and avoid the pitfall of the inability to find global minima [25].

60 Closed-form solutions, however, are not available for more complicated material models
61 under general loading conditions, which motivates the development and implementation of
62 numerical approaches. Among the works that address the numerical resolution of material
63 instability are those of Ortiz and coworkers [26, 27]. Ortiz et al. [27] formulated the detection
64 of instability as a constrained minimization problem. A two-step procedure is proposed,
65 wherein a sampling is performed over the parametric space of possible bifurcation directions
66 followed by an iterative solution scheme using a Lagrange multiplier to enforce the unit-vector
67 constraint. The algorithm was applied to the bifurcation analysis of a small deformation,
68 isotropic elastoplastic material model. Khen et al. [28] formulated the localization criterion
69 for finite deformation plasticity in a Lagrangian formulation and searched the bifurcation
70 direction using two characteristic angles in a spherical coordinate system. Boussaa and
71 Aravas [29] proposed an alternative approach where numerical and symbolic computations
72 were combined to detect the loss of strong ellipticity and applied this approach to a Gurson-
73 type porous material. Mosler [30] proposed a numerical algorithm based on sampling the
74 discrete parametric space and using the minimum of the sampling as initial guess for a
75 Newton method to find a better approximation to the exact minimum of the determinant of
76 the acoustic tensor and corresponding bifurcation directions. More recently, Oliver et al. [25]
77 developed a new efficient algorithm based on the iterative solution of a coupled eigenvalue
78 problem in terms of the acoustic tensor. The algorithm is very efficient and accurate for
79 symmetric cases, where the material tangent has both major and minor symmetries. For
80 cases that lack minor symmetries, however, the algorithm only gives an approximation, which
81 limits its applicability to finite deformation material models, or non-associative plasticity
82 material models.

83 Compared to analytical approaches, numerical algorithms are more general in the sense
84 that they can be applied to different material models under different loading conditions,
85 for both two-dimensional and three-dimensional problems. The drawbacks are also clear,
86 however: they are much more computationally demanding and less robust. The convergence
87 of an iterative method is sensitive to the initial guess, for instance. In the context of a
88 non-linear finite element analysis, the material instability condition has to be tested at every
89 integration point and at every time step, and therefore both the computational efficiency
90 and robustness of any numerical algorithm used for its detection becomes a major concern.

91 In this work, we use a sampling-based algorithm followed by a Newton iterative method
92 to solve the minimization problem associated with the strong ellipticity condition for the
93 detection of material instability. We present several parametrizations for the representation
94 of the unit normal vector used to construct the acoustic tensor. The hypothesis is that
95 the parametrization of this normal vector significantly affects the computation time and

⁹⁶ robustness of the numerical solution algorithm. To this end, we propose a new Cartesian
⁹⁷ parametrization to construct a tensor akin to the acoustic tensor and compare its performance
⁹⁸ and robustness against other four parametrizations. The numerical algorithms developed in
⁹⁹ this work are general and can be applied to both small and finite deformation material models
¹⁰⁰ with symmetric or non-symmetric tangents.

¹⁰¹ 2 General Framework

¹⁰² Incremental variational constitutive updates provide the means to determine the loss of the
¹⁰³ strong ellipticity condition for a very general class of materials. Within this framework,
¹⁰⁴ the constitutive behavior of the material during a time increment is characterized by an
¹⁰⁵ incremental stress potential that may include elasticity, viscoelasticity, viscoplasticity, and
¹⁰⁶ rate dependence [10–16].

¹⁰⁷ 2.1 Variational Constitutive Updates

¹⁰⁸ The mechanical response of the solids considered here is characterized by a dissipation po-
¹⁰⁹ tential of the form

$$D(\mathbf{F}, \dot{\mathbf{F}}, \mathbf{Z}, \dot{\mathbf{Z}}) := \dot{A}(\mathbf{F}, \mathbf{Z}) + \phi(\mathbf{F}, \dot{\mathbf{F}}, \mathbf{Z}) + \psi^*(\mathbf{Z}, \dot{\mathbf{Z}}), \quad (2.1)$$

¹¹⁰ in which $A(\mathbf{F}, \mathbf{Z})$ is the Helmholtz free-energy density, $\phi(\mathbf{F}, \dot{\mathbf{F}}, \mathbf{Z})$ is a viscous potential,
¹¹¹ $\psi^*(\mathbf{Z}, \dot{\mathbf{Z}})$ is a dual kinetic potential or dissipation function, \mathbf{F} is the deformation gradient
¹¹² and \mathbf{Z} is a collection of suitable internal variables that describe the state of the material at
¹¹³ a given point. The first Piola-Kirchhoff stress and the conjugate thermodynamic forces to
¹¹⁴ \mathbf{Z} are given by

$$\mathbf{P} := \frac{\partial D}{\partial \dot{\mathbf{F}}}(\mathbf{F}, \dot{\mathbf{F}}, \mathbf{Z}, \dot{\mathbf{Z}}) = \frac{\partial A}{\partial \mathbf{F}}(\mathbf{F}, \mathbf{Z}) + \frac{\partial \phi}{\partial \dot{\mathbf{F}}}(\mathbf{F}, \dot{\mathbf{F}}, \mathbf{Z}), \quad \mathbf{Y} := -\frac{\partial A}{\partial \mathbf{Z}}(\mathbf{F}, \mathbf{Z}), \quad (2.2)$$

¹¹⁵ respectively. In order to ensure a variational structure, we have postulated the existence of
¹¹⁶ a dual kinetic potential or dissipation function $\psi^*(\mathbf{Z}, \dot{\mathbf{Z}})$ such that

$$\mathbf{Y} = \frac{\partial \psi^*}{\partial \dot{\mathbf{Z}}}(\mathbf{Z}, \dot{\mathbf{Z}}). \quad (2.3)$$

¹¹⁷ Next, we minimize the dissipation potential (2.1) with respect to the internal variable rates
¹¹⁸ as

$$\begin{aligned} \inf_{\dot{\mathbf{Z}}} [D(\mathbf{F}, \dot{\mathbf{F}}, \mathbf{Z}, \dot{\mathbf{Z}})] &= \inf_{\dot{\mathbf{Z}}} [\dot{A}(\mathbf{F}, \mathbf{Z}) + \psi^*(\mathbf{Z}, \dot{\mathbf{Z}})] + \phi(\mathbf{F}, \dot{\mathbf{F}}, \mathbf{Z}), \\ &= \inf_{\dot{\mathbf{Z}}} \left[\frac{\partial A}{\partial \mathbf{F}}(\mathbf{F}, \mathbf{Z}) : \dot{\mathbf{F}} + \frac{\partial A}{\partial \mathbf{Z}}(\mathbf{F}, \mathbf{Z}) \cdot \dot{\mathbf{Z}} + \psi^*(\mathbf{Z}, \dot{\mathbf{Z}}) \right] + \phi(\mathbf{F}, \dot{\mathbf{F}}, \mathbf{Z}). \end{aligned} \quad (2.4)$$

¹¹⁹ This is equivalent to stating that the internal variables should not produce any net work,
¹²⁰ i.e.

$$\left[\frac{\partial A}{\partial \mathbf{Z}}(\mathbf{F}, \mathbf{Z}) + \frac{\partial \psi^*}{\partial \dot{\mathbf{Z}}}(\mathbf{Z}, \dot{\mathbf{Z}}) \right] \cdot \dot{\mathbf{Z}} = 0 \quad \forall \dot{\mathbf{Z}}, \quad (2.5)$$

¹²¹ which in turn leads to Biot's equation for standard dissipative systems

$$\frac{\partial A}{\partial \mathbf{Z}}(\mathbf{F}, \mathbf{Z}) + \frac{\partial \psi^*}{\partial \dot{\mathbf{Z}}}(\mathbf{Z}, \dot{\mathbf{Z}}) = \mathbf{0}. \quad (2.6)$$

¹²² Approximate solutions to (2.6) may be found by recourse to the incremental energy
¹²³ density function for a time increment $t \in [t_n, t_{n+1}]$

$$w(\mathbf{F}_{n+1}, \mathbf{Z}_{n+1}) := \int_{t_n}^{t_{n+1}} \left[\dot{A}(\mathbf{F}, \mathbf{Z}) + \phi(\mathbf{F}, \dot{\mathbf{F}}, \mathbf{Z}) + \psi^*(\mathbf{Z}, \dot{\mathbf{Z}}) \right] dt, \quad (2.7)$$

¹²⁴ in which the integral is evaluated using a midpoint-like rule as follows

$$\begin{aligned} w(\mathbf{F}_{n+1}, \mathbf{Z}_{n+1}) \approx & A(\mathbf{F}_{n+1}, \mathbf{Z}_{n+1}) - A(\mathbf{F}_n, \mathbf{Z}_n) + \\ & \Delta t \left[\phi \left(\mathbf{F}_{n+\alpha}, \frac{\Delta \mathbf{F}}{\Delta t}, \mathbf{Z}_{n+\alpha} \right) + \psi^* \left(\mathbf{Z}_{n+\alpha}, \frac{\Delta \mathbf{Z}}{\Delta t} \right) \right]. \end{aligned} \quad (2.8)$$

¹²⁵ with

$$\Delta t := t_{n+1} - t_n, \quad \Delta \mathbf{F} := \mathbf{F}_{n+1} \mathbf{F}_n^{-1}, \quad \Delta \mathbf{Z} := \mathbf{Z}_{n+1} - \mathbf{Z}_n, \quad (2.9)$$

¹²⁶ and

$$\begin{aligned} \mathbf{F}_{n+\alpha} &:= \exp[(1-\alpha) \log \mathbf{F}_n + \alpha \log \mathbf{F}_{n+1}], \\ \mathbf{Z}_{n+\alpha} &:= (1-\alpha) \mathbf{Z}_n + \alpha \mathbf{Z}_{n+1}, \end{aligned} \quad (2.10)$$

¹²⁷ where α is an algorithmic parameter. In order to obtain an explicit scheme, we choose $\alpha = 0$.

¹²⁸ Next, we define the incremental stress potential as

$$\begin{aligned} W(\mathbf{F}_{n+1}) &:= \inf_{\mathbf{Z}_{n+1}} [w(\mathbf{F}_{n+1}, \mathbf{Z}_{n+1})] \\ &= \inf_{\mathbf{Z}_{n+1}} \left[A(\mathbf{F}_{n+1}, \mathbf{Z}_{n+1}) - A(\mathbf{F}_n, \mathbf{Z}_n) + \Delta t \psi^* \left(\mathbf{Z}_n, \frac{\Delta \mathbf{Z}}{\Delta t} \right) \right] + \\ &\quad \Delta t \phi \left(\mathbf{F}_n, \frac{\Delta \mathbf{F}}{\Delta t}, \mathbf{Z}_n \right). \end{aligned} \quad (2.11)$$

¹²⁹ This minimization provides an optimal path for the internal variables \mathbf{Z} in the time increment
¹³⁰ $t \in [t_n, t_{n+1}]$. Furthermore, the Euler-Lagrange equation corresponding to (2.11) is

$$\frac{\partial A}{\partial \mathbf{Z}_{n+1}}(\mathbf{F}_{n+1}, \mathbf{Z}_{n+1}) + \Delta t \frac{\partial \psi^*}{\partial \mathbf{Z}_{n+1}} \left(\mathbf{Z}_n, \frac{\Delta \mathbf{Z}}{\Delta t} \right) = \mathbf{0}. \quad (2.12)$$

¹³¹ which is a discrete version of Biot's equation (2.6) [31]. The incremental first Piola-Kirchhoff
¹³² stress and tangent moduli can be computed in turn as

$$\mathbf{P}_{n+1} := \frac{\partial W}{\partial \mathbf{F}}(\mathbf{F}_{n+1}), \quad \mathbb{A}_{n+1} := \frac{\partial^2 W}{\partial \mathbf{F}^2}(\mathbf{F}_{n+1}), \quad (2.13)$$

¹³³ respectively. Thus, by using variational constitutive updates, the stress and the tangent
¹³⁴ moduli can be derived from the hyperelastic-like potential (2.11) for a very general class of
¹³⁵ constitutive behavior that may include viscosity and rate dependence. This in turn provides
¹³⁶ the means to apply the classical analysis tools that are used in hyperelasticity, such as the
¹³⁷ strong ellipticity condition, for complex inelastic materials as well.

¹³⁸ 2.2 The Strong Ellipticity Condition

¹³⁹ For simplicity in notation and unless otherwise stated, henceforth we omit the time indices
¹⁴⁰ n and $n + 1$ with the understanding that further developments take place at time t_{n+1} . The
¹⁴¹ ellipticity condition can be expressed as

$$(\mathbf{m} \otimes \mathbf{n}) : \mathbb{A} : (\mathbf{m} \otimes \mathbf{n}) \geq 0, \quad \forall \mathbf{m}, \mathbf{n} \in \mathbb{R}^3. \quad (2.14)$$

¹⁴² If the condition holds strictly for non-zero vectors \mathbf{m} and \mathbf{n} , then it is called the strong
¹⁴³ ellipticity condition [12, 17, 32]. It is customary to *assume* that \mathbf{m} and \mathbf{n} are unit vectors,
¹⁴⁴ i.e. $\mathbf{m}, \mathbf{n} \in S^2$ where $S^2 := \{\mathbf{t} \in \mathbb{R}^3 \mid \|\mathbf{t}\| = 1\}$ is the unit sphere. Define

$$\begin{aligned} \mathbf{n} \cdot \mathbb{A} &:= n_p A_{pjkl} \mathbf{e}_j \otimes \mathbf{e}_k \otimes \mathbf{e}_l, & \mathbf{n} \circ \mathbb{A} &:= n_p A_{ipkl} \mathbf{e}_i \otimes \mathbf{e}_k \otimes \mathbf{e}_l, \\ \mathbb{A} \circ \mathbf{n} &:= n_p A_{ijpl} \mathbf{e}_i \otimes \mathbf{e}_j \otimes \mathbf{e}_l, & \mathbb{A} \cdot \mathbf{n} &:= n_p A_{ijkp} \mathbf{e}_i \otimes \mathbf{e}_j \otimes \mathbf{e}_k, \end{aligned} \quad (2.15)$$

¹⁴⁵ and the acoustic tensor as

$$\mathbf{A} := \mathbf{n} \circ \mathbb{A} \cdot \mathbf{n} \quad \text{or} \quad A_{ik} \mathbf{e}_i \otimes \mathbf{e}_k := n_j A_{ijkl} n_l \mathbf{e}_i \otimes \mathbf{e}_k, \quad \mathbf{n} \in S^2, \quad (2.16)$$

¹⁴⁶ then the strong ellipticity condition becomes

$$\mathbf{m} \cdot \mathbf{A} \cdot \mathbf{m} > 0, \quad \mathbf{m} \in S^2. \quad (2.17)$$

¹⁴⁷ In order to satisfy the strong ellipticity condition, the acoustic tensor must be positive
¹⁴⁸ definite. Therefore, (2.14) and (2.17) reduce to

$$\det \mathbf{A} > 0, \quad (2.18)$$

¹⁴⁹ which provides a method to determine the onset of a material instability.

¹⁵⁰ 2.3 Bifurcation

¹⁵¹ By using the strong ellipticity condition (2.14) or its equivalent with the acoustic tensor
¹⁵² (2.18), the detection of bifurcation or loss of ellipticity in the material is fully characterized
¹⁵³ by its fourth-order tangent moduli (2.13). The onset of bifurcation is then posed as a
¹⁵⁴ minimization problem. First we assume that the normal vector \mathbf{n} is parametrized by a set
¹⁵⁵ of parameters \mathbf{q} , thus turning the determinant of the acoustic tensor $\det \mathbf{A}$ into a function
¹⁵⁶ of \mathbf{q} . Then the determinant of the acoustic tensor $\det \mathbf{A}(\mathbf{q})$ is minimized with respect to \mathbf{q} .
¹⁵⁷ Thus the loss of strong ellipticity may be stated as

$$f(\mathbf{q}) := \det \mathbf{A}(\mathbf{q}), \quad \min_{\mathbf{q}} f(\mathbf{q}) = 0, \quad \mathbf{n}(\mathbf{q}) \in S^2. \quad (2.19)$$

¹⁵⁸ If the determinant function $f(\mathbf{q})$ is differentiable, the minimization problem can be rewrite-
¹⁵⁹ ten equivalently as

$$\frac{\partial f}{\partial \mathbf{q}}(\mathbf{q}) = \mathbf{0}, \quad (2.20)$$

¹⁶⁰ which can be solved by standard numerical optimization techniques, e.g. a Newton-type it-
¹⁶¹ erative procedure.

¹⁶² 3 Parametrizations for Bifurcation Analysis

¹⁶³ Efficient computation of the minimization problem (2.20) requires a careful choice of the
¹⁶⁴ parametrization for the normal vector $\mathbf{n}(\mathbf{q}) \in S^2$, which is equivalent to selecting a parametriza-
¹⁶⁵ tion for the unit sphere. This choice has a significant effect on the complexity of the deter-
¹⁶⁶ minant function $f(\mathbf{q})$ and its derivatives with respect to \mathbf{q} needed to solve the optimization
¹⁶⁷ problem. Herein, five different options are explored. The first four (spherical, stereographic,
¹⁶⁸ projective, tangent) are indeed parametrizations of the unit sphere. The last parametriza-
¹⁶⁹ tion, which we term Cartesian, relaxes the restriction that the normal vector be an element of
¹⁷⁰ the unit sphere. We describe the parametrizations in detail next, assuming that a Cartesian
¹⁷¹ frame of reference originates from the center of each one.

¹⁷² 3.1 Spherical Parametrization

¹⁷³ This parametrization is the most commonly used in numerical bifurcation analysis, e.g. [30,
¹⁷⁴ 33–35]. In the spherical parametrization, elements \mathbf{n} of the unit sphere S^2 are simply
¹⁷⁵ parametrized by their spherical coordinates with polar angle $\varphi \in [0, \pi]$, azimuthal angle
¹⁷⁶ $\theta \in [0, \pi]$ and radial distance $r = \|\mathbf{n}\| = 1$. The reduced range in the angle θ is due to
¹⁷⁷ symmetry of the bifurcation condition, as for this purpose \mathbf{n} and $-\mathbf{n}$ yield the same result,
¹⁷⁸ see Fig. 1(a). In terms of the canonical basis

$$\mathbf{n}(\varphi, \theta) := \begin{Bmatrix} \sin \varphi \cos \theta \\ \sin \varphi \sin \theta \\ \cos \varphi \end{Bmatrix}. \quad (3.1)$$

¹⁷⁹ 3.2 Stereographic Parametrization

¹⁸⁰ The unit sphere is parametrized with the aid of an equatorial plane as shown in Fig. 1(b).
¹⁸¹ Consider a point P that is both on this plane and on a line that passes through the north
¹⁸² pole Q of the sphere and the tip of the vector \mathbf{n} . The Cartesian coordinates x and y of P
¹⁸³ provide the desired parametrization, which can be easily derived by finding the intersection
¹⁸⁴ of the line and the sphere. The upper hemisphere can be ignored due to the symmetry of the
¹⁸⁵ bifurcation condition, thus avoiding the singularity in parametrizing a normal vector that

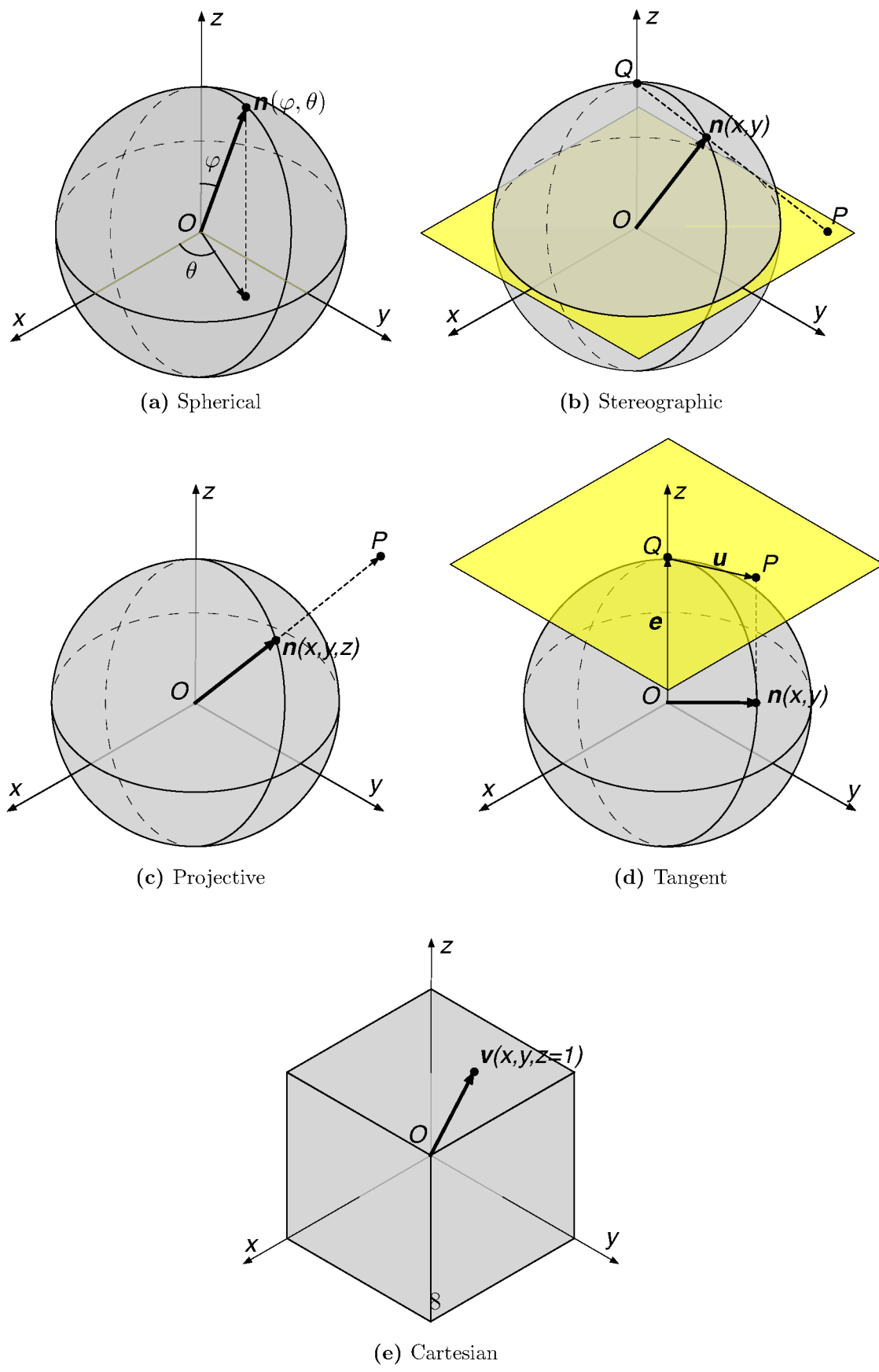


Figure 1: The five parametrizations used for the detection of loss of ellipticity.

¹⁸⁶ points to the north pole Q . The normal vector \mathbf{n} in terms of the canonical basis is

$$\mathbf{n}(x, y) := \begin{Bmatrix} \frac{2x}{x^2 + y^2 + 1} \\ \frac{2y}{x^2 + y^2 + 1} \\ \frac{x^2 + y^2 - 1}{x^2 + y^2 + 1} \end{Bmatrix}. \quad (3.2)$$

¹⁸⁷ where the parameters $x \in [-1, 1]$ and $y \in [-1, 1]$.

¹⁸⁸ 3.3 Projective Parametrization

¹⁸⁹ In the projective parametrization, the norm of the position vector of a point P with respect
¹⁹⁰ to the center of the sphere is constrained to obtain a unit vector \mathbf{n} [27]. This is equivalent
¹⁹¹ to projecting the point P onto the unit sphere S^2 , as shown in Fig. 1(c). The normalization
¹⁹² is effected by means of a constraint enforced by a Lagrange multiplier as

$$\mathbf{n}(x, y, z) := \begin{Bmatrix} x \\ y \\ z \end{Bmatrix}, \text{ subjected to } x^2 + y^2 + z^2 = 1. \quad (3.3)$$

¹⁹³ where the parameters $x \in [-1, 1]$, $y \in [-1, 1]$ and $z \in [-1, 1]$.

¹⁹⁴ 3.4 Tangent Parametrization

¹⁹⁵ This parametrization of the unit sphere is defined by a tangent plane [36]. Let $\mathbf{u} \in \mathbb{R}^3$ be
¹⁹⁶ the position vector of the point P in the tangent plane with respect to the contact point
¹⁹⁷ Q between the sphere and the plane, then let $\mathbf{e} \in S^2$ be the position vector of the contact
¹⁹⁸ point Q with respect to the center of the sphere O , as shown in Fig. 1(d). Define a rotation
¹⁹⁹ vector $\boldsymbol{\theta} := \mathbf{e} \times \mathbf{u}$, then the rotation angle is $\theta := \|\boldsymbol{\theta}\| \equiv \|\mathbf{u}\|$. Let also $\check{\boldsymbol{\theta}} \in so(3)$ be the
²⁰⁰ skew-symmetric tensor such that $\check{\boldsymbol{\theta}} \cdot \mathbf{v} \equiv \boldsymbol{\theta} \times \mathbf{v} \forall \mathbf{v} \in \mathbb{R}^3$. The expression for the exponential
²⁰¹ map for $\check{\boldsymbol{\theta}}$ is

$$\exp \check{\boldsymbol{\theta}} := \begin{cases} \mathbf{I} \in SO(3), & \text{if } \theta = 0; \\ \mathbf{I} + \frac{\sin \theta}{\theta} \check{\boldsymbol{\theta}} + \frac{(1 - \cos \theta)}{\theta^2} \check{\boldsymbol{\theta}}^2 \in SO(3), & \text{if } \theta > 0; \end{cases} \quad (3.4)$$

²⁰² which is often accredited to Rodrigues [37]. Next define

$$\exp_{\mathbf{e}} \mathbf{u} := \exp \check{\boldsymbol{\theta}} \cdot \mathbf{e} = \cos \theta \mathbf{e} + \frac{\sin \theta}{\theta} \mathbf{u} \in S^2. \quad (3.5)$$

²⁰³ The parametrization follows immediately by setting the contact point Q to the north pole
²⁰⁴ of the sphere, i.e. $\mathbf{e} = [0, 0, 1]^T$ and $\mathbf{u} = [x, y, 0]^T$ with the normal vector \mathbf{n} given by

$$\mathbf{n} = \exp_{\mathbf{e}} \mathbf{u} \in S^2. \quad (3.6)$$

²⁰⁵ which leads to a more explicit representation for the normal vector in the canonical basis as

$$\mathbf{n}(x, y) := \begin{Bmatrix} \frac{x \sin \sqrt{x^2 + y^2}}{\sqrt{x^2 + y^2}} \\ \frac{y \sin \sqrt{x^2 + y^2}}{\sqrt{x^2 + y^2}} \\ \cos \sqrt{x^2 + y^2} \end{Bmatrix}. \quad (3.7)$$

²⁰⁶ where the parameters $x \in [-\pi/2, \pi/2]$ and $y \in [-\pi/2, \pi/2]$

²⁰⁷ 3.5 Cartesian Parametrization

²⁰⁸ The previous four are parametrizations of the unit sphere. Here, we propose a new parametrization,
²⁰⁹ termed Cartesian, where the restriction that the normal vector be of unit length is
²¹⁰ relaxed. To set the stage for the Cartesian parametrization, we revisit the strong ellipticity
²¹¹ condition

$$(\mathbf{u} \otimes \mathbf{v}) : \mathbb{A} : (\mathbf{u} \otimes \mathbf{v}) > 0, \quad \forall \mathbf{u}, \mathbf{v} \in \mathbb{R}^3 \setminus \{\mathbf{0}\} \quad (3.8)$$

²¹² Note that this condition only requires that the vectors \mathbf{u} and \mathbf{v} be non-zero. Thus, the
²¹³ condition that they belong to the unit sphere S^2 may be relaxed. In analogy to the classical
²¹⁴ acoustic tensor (2.16), define

$$\mathbf{B} := \mathbf{v} \circ \mathbb{A} \cdot \mathbf{v} \quad \text{or} \quad B_{ik} \mathbf{e}_i \otimes \mathbf{e}_k := v_j A_{ijkl} v_l \mathbf{e}_i \otimes \mathbf{e}_k, \quad \mathbf{v} \in \mathbb{R}^3 \setminus \{\mathbf{0}\}, \quad (3.9)$$

²¹⁵ thus the strong ellipticity condition may be expressed as

$$\mathbf{u} \cdot \mathbf{B} \cdot \mathbf{u} > 0, \quad \mathbf{u} \in \mathbb{R}^3 \setminus \{\mathbf{0}\}. \quad (3.10)$$

²¹⁶ As in (2.18), the strong ellipticity condition becomes

$$\det \mathbf{B} > 0. \quad (3.11)$$

²¹⁷ **Proposition 1.** *The tensor \mathbf{B} from (3.9) leads to the same bifurcation condition as the
²¹⁸ acoustic tensor \mathbf{A} from (2.16), i.e., if the minimum for $\det \mathbf{A}$ is equal to zero for a vector
²¹⁹ $\mathbf{a} \in S^2$, then the minimum for $\det \mathbf{B}$ is also zero for a vector $\mathbf{b} \in \mathbb{R}^3 \setminus \{\mathbf{0}\}$ that is parallel to
²²⁰ \mathbf{a} .*

²²¹ *Proof.* Introduce the bijective map $g : \mathbb{R}^3 \setminus \{\mathbf{0}\} \mapsto S^2 \times \mathbb{R}^+$ that allows the representation
²²² of nonzero vectors in \mathbb{R}^3 as unit vectors in the unit sphere (direction) and the corresponding
²²³ nonzero norm (magnitude). Then define

$$\mathbf{v} \in \mathbb{R}^3 \setminus \{\mathbf{0}\}, \quad v := \|\mathbf{v}\| \in \mathbb{R}^+, \quad \mathbf{n} := \frac{\mathbf{v}}{v} \in S^2, \quad (3.12)$$

²²⁴ therefore from (2.17) and (3.10)

$$\mathbf{B}(v, \mathbf{n}) = v^2 \mathbf{A}(\mathbf{n}) \quad \text{and} \quad \det \mathbf{B}(v, \mathbf{n}) = v^6 \det \mathbf{A}(\mathbf{n}). \quad (3.13)$$

²²⁵ Now let the bifurcation condition for \mathbf{A} be

$$\min_{\mathbf{n}} \det \mathbf{A}(\mathbf{n}) = 0, \quad \mathbf{a} := \arg \min_{\mathbf{n}} \det \mathbf{A}(\mathbf{n}) \in S^2 \implies \det \mathbf{A}(\mathbf{n}) > 0 \forall \mathbf{n} \neq \mathbf{a}, \quad (3.14)$$

²²⁶ then it follows from (3.13) that

$$\det \mathbf{B}(s, \mathbf{a}) = 0, \quad \det \mathbf{B}(s, \mathbf{n}) > 0, \quad \forall \mathbf{n} \neq \mathbf{a} \text{ and } \forall s \in \mathbb{R}^+, \quad (3.15)$$

²²⁷ which means that

$$\min_{v, \mathbf{n}} \det \mathbf{B}(v, \mathbf{n}) = 0, \quad \{s, \mathbf{a}\} := \arg \min_{v, \mathbf{n}} \det \mathbf{B}(v, \mathbf{n}) \forall s \in \mathbb{R}^+, \quad (3.16)$$

²²⁸ as required. \square

²²⁹ In order to remove the multiple minima associated with the arbitrary value of the scalar
²³⁰ parameter s and obtain a parametrization, we restrict the range of the Cartesian coordinates
²³¹ such that $\|\mathbf{v}\|_\infty = 1$ and set the normal vector to

$$\mathbf{v}(x, y, z) := \begin{cases} [x, y, 1]^T, & \text{if } x \in [-1, 1] \text{ and } y \in [-1, 1]; \\ [1, y, z]^T, & \text{if } y \in [-1, 1] \text{ and } z \in [-1, 1]; \\ [x, 1, z]^T, & \text{if } z \in [-1, 1] \text{ and } x \in [-1, 1]; \\ [1, 1, 1]^T, & \text{otherwise.} \end{cases} \quad (3.17)$$

²³² This confines the normal vector to the cube of side length two centered at the origin as
²³³ shown in Fig. 1(e). Only three faces of the cube need to be considered due to the symmetry
²³⁴ of the bifurcation condition.

²³⁵ The spherical parametrization commonly used in bifurcation analysis has a singularity
²³⁶ at the poles as the azimuthal angle θ can adopt any value at those points. This leads to
²³⁷ numerical difficulties when minima lie near or at the poles. The Cartesian parametrization
²³⁸ advocated here does not contain any singularities of this kind.

²³⁹ 4 Bifurcation Detection

²⁴⁰ Within an incremental update setting, the numerical detection of the bifurcation condition
²⁴¹ for each time increment using any of the parametrizations just described consists of the
²⁴² following two steps:

- ²⁴³ • An initial sampling is performed over the parametric space for \mathbf{q} for the normal vector
²⁴⁴ $\mathbf{n} \in S^2$ or $\mathbf{v} \in \{\mathbf{u} \in \mathbb{R}^3 | \|\mathbf{u}\|_\infty = 1\}$ associated with the parametrization. This leads to
²⁴⁵ a rough estimate of the minimum of the determinant function (2.19) and the associated
²⁴⁶ bifurcation directions.
- ²⁴⁷ • The coarse estimate can be used to initiate an iterative procedure to find a more
²⁴⁸ accurate estimate of the onset of bifurcation and its associated directions by solving
²⁴⁹ the optimization problem (2.20).

250 In an actual finite element simulation, the above two-step procedure may not yield es-
 251 timates of the bifurcation condition that are accurate enough within a time increment, in
 252 particular if the size of the increment is relatively large. One way to improve the solution is
 253 to introduce adaptive time increments for the detection of the bifurcation condition. Define

$$\mu_{n+1,k} := \min_{\mathbf{q}} f_{n+1,k}(\mathbf{q}) = \min_{\mathbf{q}} \det \mathbf{B}_{n+1,k}(\mathbf{q}) \quad (4.1)$$

254 where the tensor $\mathbf{B}_{n+1,k}(\mathbf{q})$ may be either the one from (2.16) or the one from (3.9), depending
 255 on the parametrization in use, and the index $n + 1, k$ indicates that the evaluation occurs at
 256 time $t_{n+1,k} \in [t_n, t_{n+1}]$ for a k -th adaptive iteration.

257 Consider the original time increment from t_n to t_{n+1} , where $\mu_n > 0$ and $\mu_{n+1} < 0$. This
 258 means that between time t_n and t_{n+1} , the strong ellipticity condition is violated and hence
 259 the material exhibits bifurcation. Assume also that $\mu_n/\mu_0 > \epsilon$, where μ_0 is the value of the
 260 determinant function evaluated at time t_0 and ϵ is a target tolerance. We wish to find a
 261 better estimate for the determinant function $\mu_{n+1,k}$, and hence the bifurcation time $t_{n+1,k}$,
 262 such that $\mu_{n+1,k}/\mu_0 \leq \epsilon$. This is achieved by an adaptive time increment procedure by
 263 means of bisection, as shown in Algorithm 1. This algorithm repeatedly decreases the time
 264 increment in half until the convergence criterion $\mu_{n+1,k}/\mu_0 \leq \epsilon$ is met.

Algorithm 1 AdaptiveStep($\mu_0, \mu_{n+1}, t_{n+1}, \epsilon$)

Require: $\mu_{n+1} < 0$

Ensure: $\mu_{n+1,k} \in [0, \epsilon\mu_0]$

initialize $k \leftarrow 1$, $\alpha \leftarrow \frac{1}{2}$, $\Delta t \leftarrow t_{n+1} - t_n$, $\mu_{n+1,k} \leftarrow \mu_{n+1}$

while $\mu_{n+1,k} < 0$ or $\mu_{n+1,k}/\mu_0 > \epsilon$ **do**

$t_{n+1,k} \leftarrow t_n + \alpha \Delta t$

 compute $\mathbf{F}(t_{n+1,k})$ using the global solution scheme

 compute $\Delta \mathbf{Z}(t_{n+1,k})$ by solving (2.12)

 compute $\mathbb{A}(t_{n+1,k})$ using (2.13)

 compute $\mu_{n+1,k}$ by solving (4.1)

if $\mu_{n+1,k} > 0$ **then**

$\alpha \leftarrow \alpha + 2^{-k-1}$

else

$\alpha \leftarrow \alpha - 2^{-k-1}$

end if

$k \leftarrow k + 1$

end while

265 The adaptive time increment procedure allows the accurate (up to the tolerance ϵ) de-
 266 tection of the bifurcation time during a loading process. The procedure described in this
 267 section to detect material bifurcation can be applied to a very general class of materials and
 268 its numerical performance is demonstrated in the following section.

269 5 Numerical Examples

270 The performance and applicability of the proposed Cartesian and the other four parametrizations
 271 are examined by using them for the bifurcation analysis of two material models under
 272 different loading conditions. The analysis is performed at the material point level. Of particu-
 273 lar interest are the robustness and computational efficiency of the different parametrizations.

274 5.1 Small Deformation Isotropic Elastic Damage Model

275 We start the bifurcation analysis on a simple small deformation isotropic damage model.
 276 The model formulation is briefly presented first. The material model is then subjected to
 277 simple shear to determine the performance of the different parametrizations on the detection
 278 of material bifurcation.

279 5.1.1 Model Formulation

280 The stress and constitutive tangent of the small deformation isotropic damage model are
 281 derived from the strain-energy function that has the form

$$282 A(\epsilon^e, \xi) := \frac{1}{2}(1 - \xi)\epsilon^e : \mathbb{C}^e : \epsilon^e \quad (5.1)$$

282 where ϵ^e is the infinitesimal elastic strain tensor, \mathbb{C}^e is the fourth-order elastic moduli tensor,
 283 and ξ is a damage parameter introduced to trigger material bifurcation. For isotropic linear
 284 elasticity, the elastic moduli tensor \mathbb{C}^e is given as

$$\mathbb{C}^e := \lambda \mathbf{I} \otimes \mathbf{I} + 2\mu \mathbb{I} \quad (5.2)$$

285 where λ and μ are the Lamé constants, \mathbf{I} is the second-order identity tensor and $(\mathbb{I})_{ijkl} =$
 286 $\frac{1}{2}(\delta_{ik}\delta_{jl} + \delta_{il}\delta_{jk})$ is the fourth-order symmetric identity tensor with δ_{ik} being the Kronecker
 287 delta.

288 We adopt the following evolution law for the scalar damage parameter ξ [38]

$$\xi(\alpha) := \xi_\infty [1 - \exp(-\alpha/\tau)] \quad (5.3)$$

289 where ξ_∞ describes the dimensionless maximum damage and τ is referred to as the damage
 290 saturation parameter. The parameter α is the maximum thermodynamic force [38] with the
 291 same dimensions as the effective strain energy. Within the closed time interval $[0, t]$, α is
 292 given as

$$\alpha(t) := \max_{s \in [0, t]} A_0(s) \quad (5.4)$$

293 where $A_0(s)$ is the undamaged strain energy at time s .

294 Given the strain-energy function (5.1) and the damage evolution (5.3), the fourth-order
 295 tangent moduli tensor can be obtained by differentiating the strain-energy function with
 296 respect to the strain measure ϵ^e twice, which results in

$$\mathbb{C} := (1 - \xi)\mathbb{C}^e - \beta \frac{\partial \xi}{\partial \alpha} (\boldsymbol{\sigma}_0 \otimes \boldsymbol{\sigma}_0) \quad (5.5)$$

²⁹⁷ where σ_0 is the effective (undamaged) Cauchy stress and $\beta = 1 \Leftrightarrow \dot{\alpha} > 0$, $\beta = 0$ otherwise.
²⁹⁸ In a small deformation setting, this tangent can be used to compute the acoustic tensor
²⁹⁹ (2.16), which can then be tested for material bifurcation.

³⁰⁰ 5.1.2 Simple Shear Test

³⁰¹ In this section, a simple shear test illustrated in Figure 2 is simulated with the following
³⁰² material properties: $\lambda = 80$, $\mu = 80$, $\xi_\infty = 1.0$ and $\tau = 1.0$. The resulting shear stress
³⁰³ and shear strain are plotted in Fig. 3(a). The softening response is due to the evolution of
the introduced damage parameter ξ . For the numerical detection of material bifurcation, the

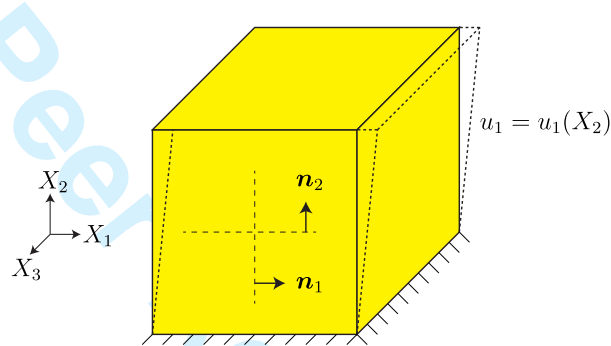


Figure 2: Schematic of the applied loading for simple shear for infinitesimal deformations. The solution bifurcates on planes with normals \mathbf{n}_1 and \mathbf{n}_2 .

³⁰⁴ two-step procedure described in Sec. 4 is adopted, i.e., (1) an initial sampling performed over
³⁰⁵ the parametric space, and (2) a Newton iterative procedure to obtain a better estimate of
³⁰⁶ the onset of bifurcation and its associated directions. Fig. 3(b) shows the degradation of the
³⁰⁷ determinant $\det \mathbf{A}$ for all five parametrizations up to the point when material bifurcation
³⁰⁸ is detected. When $\det \mathbf{A} = 0$, the material model bifurcates. In this example, all five
³⁰⁹ parametrizations detect bifurcation at the same time, i.e., when the shear strain $\epsilon_{12} = 0.0559$
³¹⁰ as marked in Fig. 3 (a). With the adaptive time step algorithm the precise time of bifurcation,
³¹¹ up to the specified tolerance, can be detected.
³¹²

³¹³ While all five parametrizations detect bifurcation at the same time, Fig. 3(b) provides
³¹⁴ little information on their computational efficiency and robustness, which are the focus of this
³¹⁵ work. The computation time of bifurcation detection mainly consists of two parts: (1) the
³¹⁶ computation time of the initial sampling over the parametric space, and (2) the computation
³¹⁷ time of the Newton iterative scheme.

³¹⁸ The computation time of the initial sampling depends on the number of sampling points,
³¹⁹ or equivalently, the density of the initial sampling grid. The denser the initial sampling grid,
³²⁰ the more expensive it is computationally to perform a complete pass of all the points in the
³²¹ grid. The computation time for the Newton iterative scheme, on the other hand, depends
³²² mainly on the complexity of the objective function, i.e., $\det \mathbf{A}$, as well as the quality of the
³²³ initial guess.

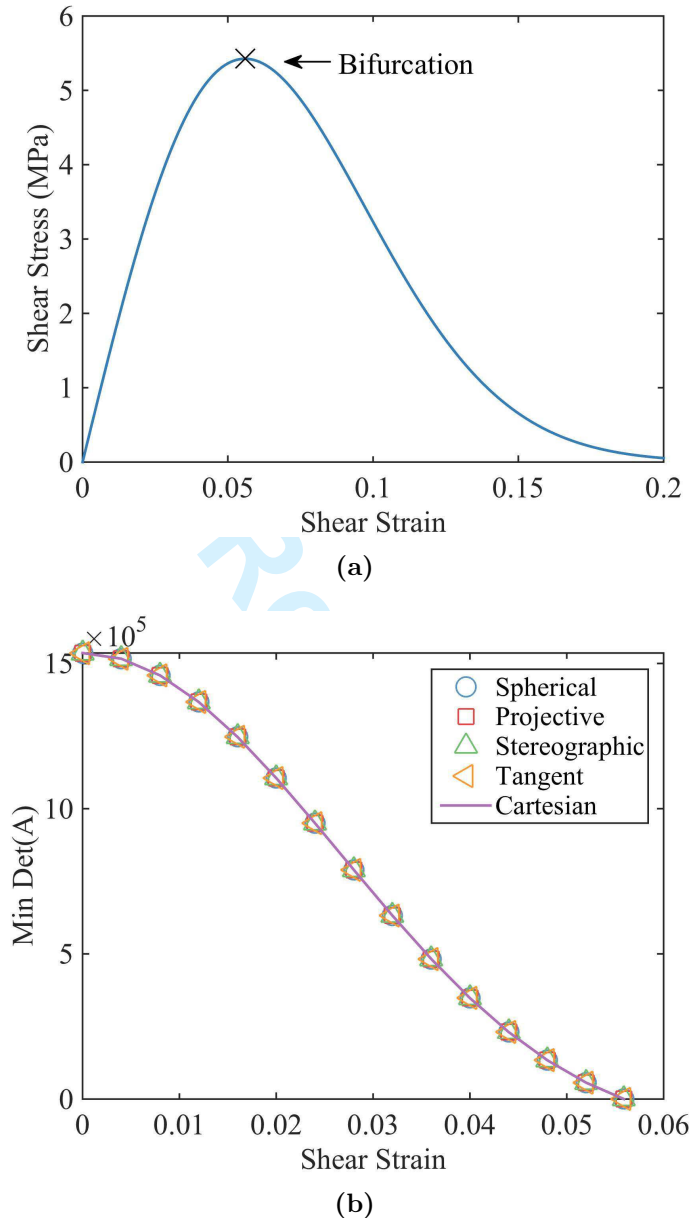


Figure 3: Simple shear test on small deformation isotropic damage model: (a) stress strain behavior, with the X indicating bifurcation, and (b) degradation of $\det \mathbf{A}$ for different parametrizations upto the point material bifurcates ($\epsilon_{12} = 0.0559$).

324 To compare the computation times of different parametrizations, we record the time spent
 325 on the bifurcation detection at a particular loading increment, e.g., at the increment leading
 326 to bifurcation. We also vary the density of the initial sampling grid to determine its effect
 327 on different parametrizations. The density of the initial sampling grid is represented by the
 328 sampling interval and the number of sampling points, as shown in Fig. 4.

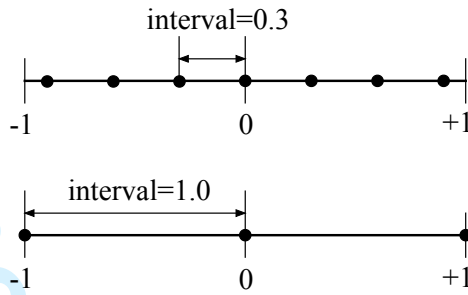


Figure 4: Schematic drawing shows the interval along one dimension of the normalized parameter space $[-1, 1]$ for the cases of interval = 0.3 (top) and interval = 1.0 (bottom). Black solid circles indicate the locations of grid points

329 A robust parametrization should be insensitive to the initial sampling grid. The computa-
 330 tion time results are summarized in Table 1. The table only shows the number of sampling
 331 points, N , along one dimension of the parametric space. Assuming the same number of inter-
 332 vals for each parameter, the total number of sampling points is N^D where D is the total
 333 dimension of the parametric space.

334 As expected, it can be seen from Table 1 that as the number of sampling points N
 335 per dimension decreases, so does the computation time. The spherical and the Car-
 336 teian parametrizations are the most efficient. The stereographic, projective and tangent
 337 parametrizations are more computationally expensive. In the extreme case with $N = 1$
 338 i.e. only one initial sampling point, the stereographic, projective and tangent parametriza-
 339 tions fail to correctly detect bifurcation, shown as a dash in the table.

340 As mentioned before, the choice of parametrization directly affects the complexity of
 341 the objective function $\det \mathbf{A}$ in (2.20). This in turn affects the computational efficiency
 342 and robustness of the different parametrizations for the detection of material bifurcation, as
 343 shown in Table 1. To illustrate this point, the landscapes of the objective function $\det \mathbf{A}$ at
 344 bifurcation, i.e., at $\epsilon_{12} = 0.0559$ are shown in Fig. 5. The corresponding plane views of the
 345 determinant landscapes are shown in Fig. 6, where the white stars indicate global minima.
 346 The projective parametrization requires three parameters and therefore it is not shown.

347 It is clear from these landscape plots that the complexity of the shape of the determinant
 348 function depends greatly on the choice of parametrization. Even for the very simple small
 349 deformation isotropic model adopted in this example, the landscape of the determinant
 350 function can be quite complex as in the cases of the spherical, stereographic and tangent
 351 parametrizations.

352 The Cartesian parametrization results in a simple bowl-shaped objective function, which

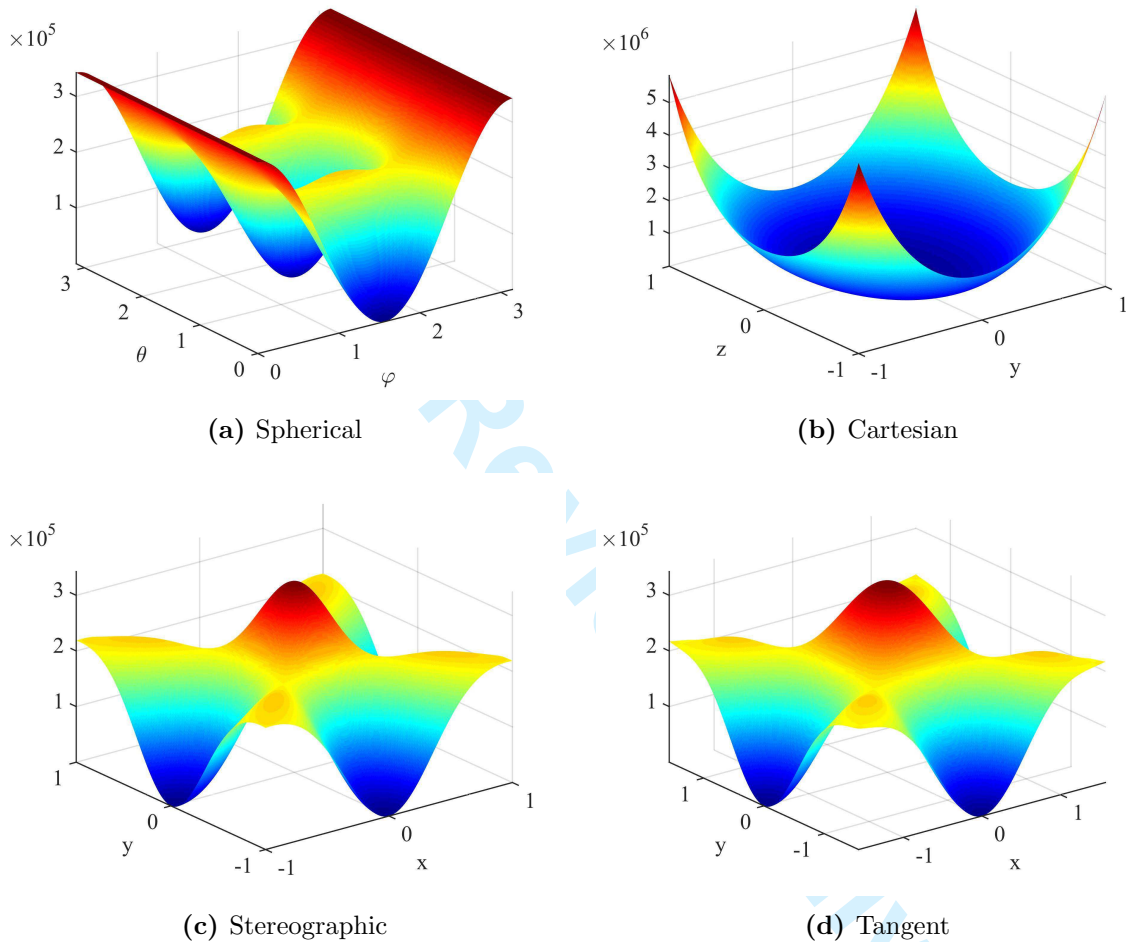


Figure 5: Landscapes of the determinant of the acoustic tensor at bifurcation for simple shear for the small deformation isotropic damage model. The normals to the planes of bifurcation are $\mathbf{n}_1 = (1, 0, 0)$ and $\mathbf{n}_2 = (0, 1, 0)$.

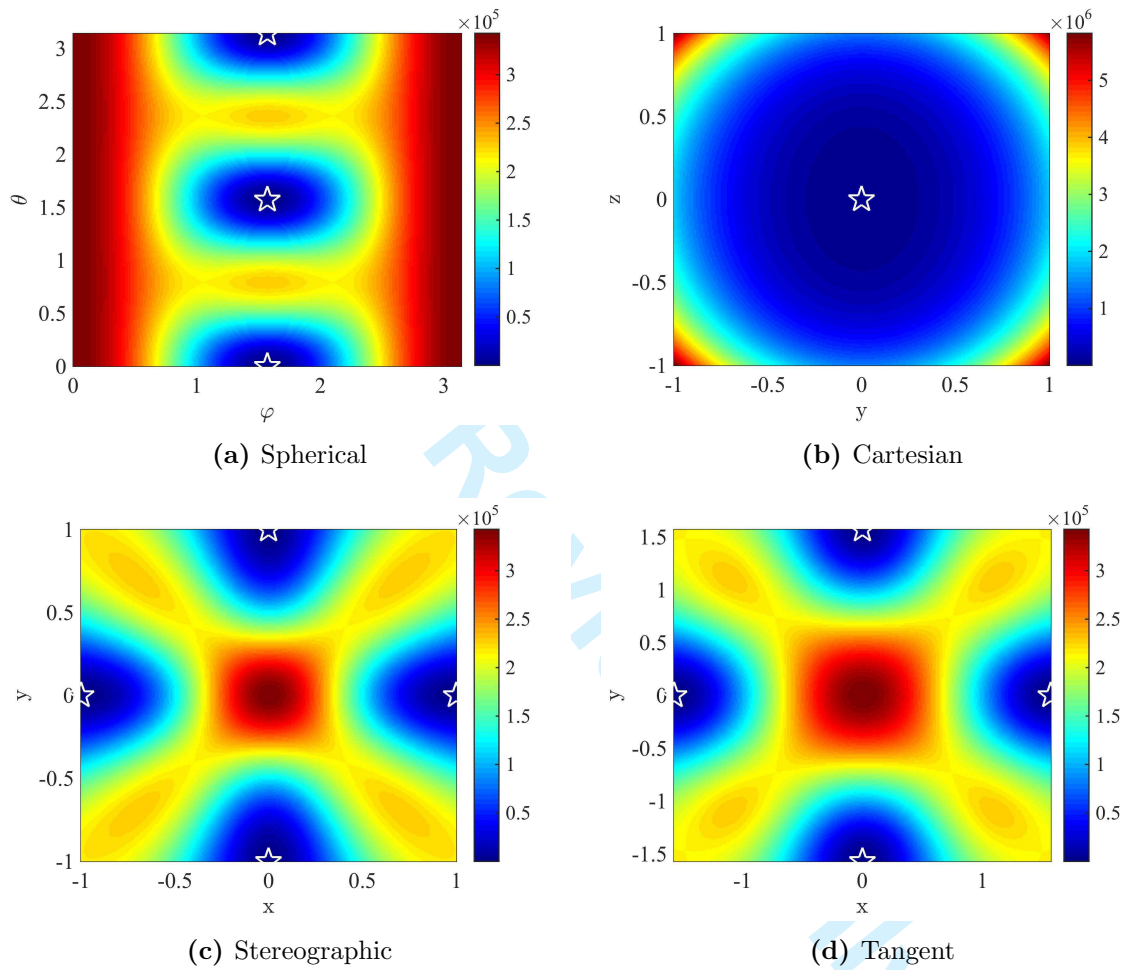


Figure 6: Plane views of the landscapes of the determinant of the acoustic tensor at bifurcation for simple shear on the small deformation isotropic damage model. The white stars indicate global minima. The normals to the planes of bifurcation are $\mathbf{n}_1 = (1, 0, 0)$ and $\mathbf{n}_2 = (0, 1, 0)$.

Sampling Interval	Points	Run Time (μ s)				
		Spherical	Stereographic	Projective	Tangent	Cartesian
0.05	41	318	155	5636	226	347
0.1	21	124	89	884	107	115
0.2	11	70	60	183	64	81
0.3	7	63	184	178	157	39
0.4	5	73	181	197	145	27
0.5	5	51	37	88	53	27
0.6	3	62	174	200	215	23
0.7	3	61	180	188	188	23
0.8	3	50	170	188	144	24
0.9	3	51	177	156	159	23
1.0	3	47	37	79	51	23
1.5	1	51	—	—	—	21

Table 1: Computation time of the different parametrizations for the simple shear test in the loading increment leading to bifurcation. The dash “—” indicates that the parametrization fails to detect bifurcation in this loading increment.

353 renders the Newton iterative scheme to be particularly robust and insensitive to the initial
 354 guess. Evidence for this can be seen in Table 1 as the Cartesian and spherical parametriza-
 355 tions are the only ones able to detect bifurcation when the sampling grid is reduced to a
 356 single point.

357 We now elaborate further on the robustness of the parametrizations by considering the
 358 situation in which the initial sampling is eliminated altogether. In the absence of the initial
 359 sampling, a random point within the corresponding parametric space is provided as initial
 360 guess for the Newton iterative scheme when $\epsilon_{12} = 0.0559$, i.e., at the onset of bifurcation. If
 361 Algorithm 1 is able to correctly detect the onset of bifurcation and its associated directions,
 362 the parametrization is said to succeed for this one set of randomly generated parameters.
 363 This process is repeated 1000 times for each parametrization.

364 Table 2 shows the rate of successful bifurcation detection for all five parametrizations. The
 365 average number of iterations and the computation time of those successful detections are also
 366 recorded and shown in the table. It can be seen that the proposed Cartesian parametrization
 367 is much more robust than the commonly used spherical parametrization, cf. 100% vs. 12.8%
 368 success rate. Furthermore, the Cartesian parametrization also outperforms the remaining
 369 three parametrizations. In terms of computation time, the Cartesian parametrization is
 370 efficient with respect to the other tested parametrizations due to its average run time of
 371 207 μ s.

372 The better performance of the proposed Cartesian parametrization in terms of com-
 373 putational efficiency and robustness can be attributed to its relatively simple determinant
 374 function landscape. Fig. 7 shows contours of the determinant functions corresponding to

	Spherical	Stereographic	Projective	Tangent	Cartesian
Success rate (%)	12.8	22.7	59.9	20.6	100
Average iteration count	4.39	4.70	8.86	5.12	5.35
Average run time (μs)	211	242	495	264	207

Table 2: Isotropic small deformation model: success rate and computation time of the Newton iterative scheme with a single random initial point. A total of 1000 random trials are performed for each parametrization. Note that the average run time is for successful bifurcation detections only, which is 100% for the Cartesian parametrization.

³⁷⁵ Table 2. One thousand random initial points are also plotted. If the initial guess leads to
³⁷⁶ a successful detection of bifurcation and its directions, the point is marked as a solid circle
³⁷⁷ (\bullet). Otherwise, it is marked as a cross (\times). This figure provides a very direct visualization
³⁷⁸ of the robustness results.

³⁷⁹ 5.2 Finite Deformation Anisotropic Hyperelastic Damage Model

³⁸⁰ The second material model tested is a finite deformation anisotropic hyperelastic damage
³⁸¹ model. Our aim is to study the effect of adding complexity to the material model, and hence
³⁸² the tangent moduli, on the performance of the different parametrizations. As in the previous
³⁸³ example, we first present the key features of the material model.

³⁸⁴ 5.2.1 Model Formulation

³⁸⁵ The free energy function of the finite deformation anisotropic hyperelastic damage model
³⁸⁶ consists of an isotropic term and direction-dependent terms. The motivation for this type
³⁸⁷ of energy formulation is to capture the behavior of materials with an isotropic matrix and
³⁸⁸ embedded microfibers with preferred directions, such as the model proposed by Chen et al.
³⁸⁹ [39] to describe the behavior of cladding for nuclear reactors subjected to damage by hydride
³⁹⁰ compounds. We assume that the damage affects both the matrix and the microfibers. The
³⁹¹ free energy function is assumed to have the form

$$A(\mathbf{C}, \mathbf{M}, \xi^m, \xi_i^f) := (1 - \xi^m) f^m \Psi^m(\mathbf{C}) + \sum_{i=1}^N (1 - \xi_i^f) f_i^f \Psi_i^f(\mathbf{C}, \mathbf{M}) \quad (5.6)$$

³⁹² where \mathbf{C} is the right Cauchy-Green tensor, \mathbf{M} is a unit vector characterizing the preferred
³⁹³ fiber direction, f^m and f_i^f are the volume fraction of the matrix and i th fiber, N is the
³⁹⁴ number of fiber terms and ξ^m and ξ_i^f are the damage factors corresponding to the matrix
³⁹⁵ and the i -th fibers, respectively. In the following examples, we assume that there are two
³⁹⁶ preferred fiber directions.

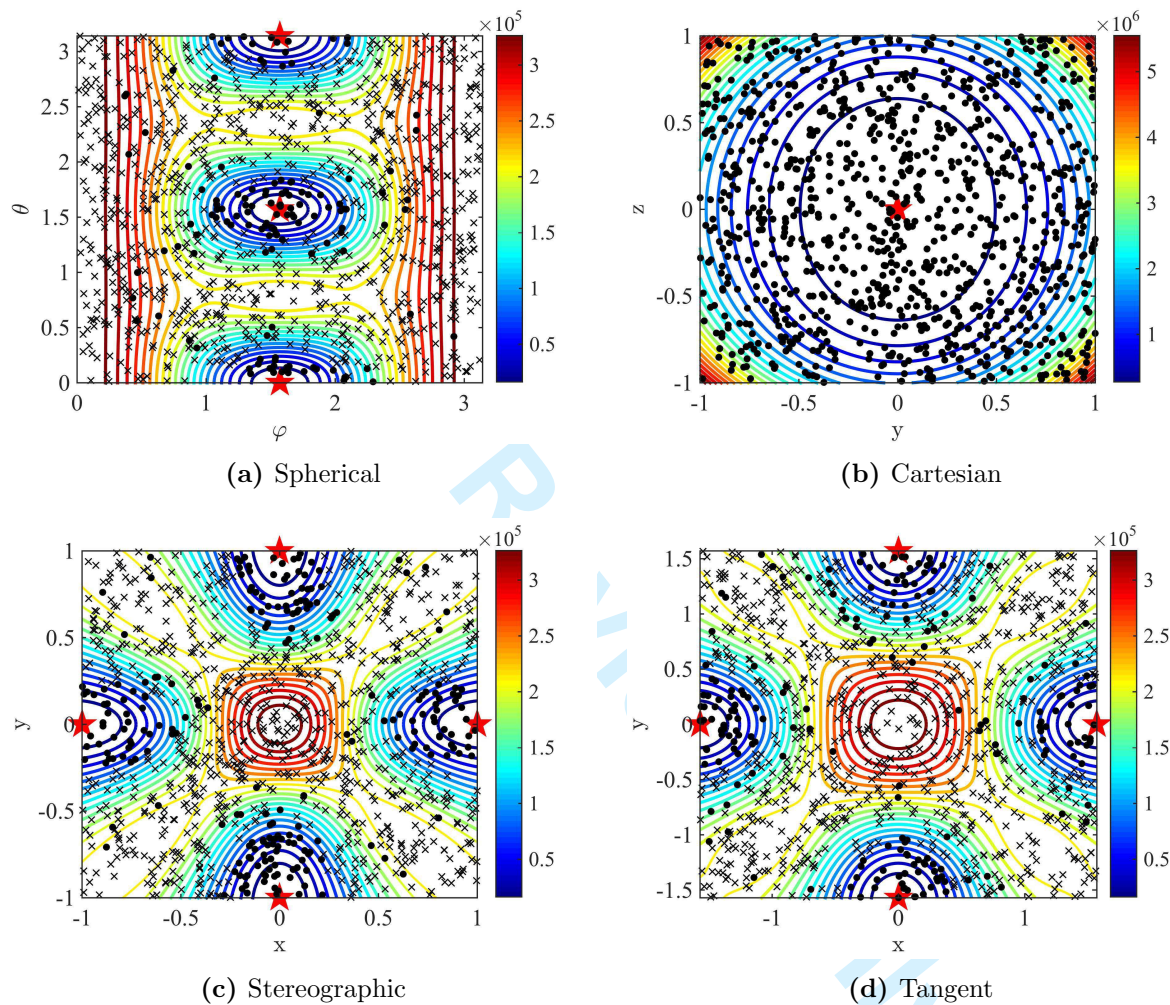


Figure 7: Isotropic small deformation model: results of the Newton iterative scheme with a single random initial guess plotted on contours of the determinant function at bifurcation. A solid circle (\bullet) indicates that the initial point leads to a successful detection of bifurcation and its directions. A cross (\times) indicates failure. A total of 1000 random trials are performed for each parametrization.

³⁹⁷ We adopt a compressible Neo-Hookean type energy function for the effective (undamaged)
³⁹⁸ matrix component

$$\Psi^m(\mathbf{C}) = \frac{1}{8}\lambda(\log I_3)^2 - \frac{1}{2}\mu \log I_3 + \frac{1}{2}\mu(I_1 - 3) \quad (5.7)$$

³⁹⁹ where λ and μ play the role of the Lamé constants of linear elasticity. For the microfibers we
⁴⁰⁰ adopt the particular form of strain-energy function proposed by Holzapfel and Ogden [40]

$$\Psi_i^f(\mathbf{C}, \mathbf{M}) = \frac{k_i}{q_i} \{\exp[q_i(I_4 - 1)^2]\} \quad (5.8)$$

where k_i and q_i are elastic constants for the i -th fiber. The strain invariants I_1 , I_3 and I_4 are defined as

$$I_1 = \text{tr } \mathbf{C}, \quad I_3 = \det \mathbf{C}, \quad I_4 = \mathbf{M} \cdot \mathbf{C} \cdot \mathbf{M}. \quad (5.9)$$

⁴⁰¹ For the damage parameters, the same evolution law as in (5.3) is used, except that for each
⁴⁰² phase of the material, there is a different set of parameters as discussed in Chen et al. [39].

⁴⁰³ Given the energy function (5.6), the fourth-order tangent moduli tensor can be derived
⁴⁰⁴ as

$$\mathbb{C} := (1 - \xi^m)\mathbb{C}^m - \beta^m \xi^{m'} (\mathbf{S}^m \otimes \mathbf{S}^m) + \sum_{i=1}^N \left[(1 - \xi_i^f) \mathbb{C}_i^f - \beta_i^f \xi_i^{f'} (\mathbf{S}_i^f \otimes \mathbf{S}_i^f) \right] \quad (5.10)$$

⁴⁰⁵ where $\beta^m = 1$ if the damage of the matrix evolves within the time increment or $\beta^m = 0$
⁴⁰⁶ otherwise; $\beta_i^f = 1$ if the damage of the i -th fiber evolves within the time increment or
⁴⁰⁷ $\beta_i^f = 0$ otherwise; $\xi^{m'}$ and $\xi_i^{f'}$ are the derivatives of the damage parameters defined in (5.3)
⁴⁰⁸ with respect to the maximum thermodynamic force defined in (5.4); and \mathbf{S}^m and \mathbf{S}_i^f are the
⁴⁰⁹ effective (undamaged) second Piola-Kirchhoff stresses for the matrix and the i -th fibers given
⁴¹⁰ by

$$\mathbf{S}^m := 2f^m \frac{\partial \Psi^m}{\partial \mathbf{C}} \quad (5.11)$$

⁴¹¹ and

$$\mathbf{S}_i^f := 2f_i^f \frac{\partial \Psi_i^f}{\partial \mathbf{C}} \quad (5.12)$$

⁴¹² where f^m and f_i^f are the volume fraction of the matrix and i -th fiber, respectively.

⁴¹³ The effective tangent moduli tensors can be calculated as

$$\mathbb{C}^m := 2 \frac{\partial \mathbf{S}^m}{\partial \mathbf{C}} \quad (5.13)$$

⁴¹⁴ and

$$\mathbb{C}_i^f := 2 \frac{\partial \mathbf{S}_i^f}{\partial \mathbf{C}}. \quad (5.14)$$

⁴¹⁵ It should be noted that the fourth-order tangent \mathbb{C} from (5.10) is computed as the second
⁴¹⁶ derivative of the strain energy with respect to the right Cauchy-Green deformation tensor \mathbf{C} .

⁴¹⁷ The strong ellipticity condition (2.14) requires the tangent \mathbb{A} that is obtained as the second
⁴¹⁸ derivative of the strain energy with respect to the deformation gradient \mathbf{F} . One tangent can
⁴¹⁹ be converted to the other using the following relation (in indicial notation)

$$\mathbb{A}_{ijkl} = S_{lj}\delta_{ik} + F_{ip}\mathbb{C}_{pjql}F_{kq} \quad (5.15)$$

⁴²⁰ where S_{lj} are the components of the second Piola-Kirchhoff stress (including damage con-
⁴²¹ tribution) of the corresponding phase (e.g., matrix or fiber component), δ_{ik} is the Kronecker
⁴²² delta and F_{ij} are the components of the deformation gradient.

⁴²³ 5.2.2 Uniaxial Tension Test

⁴²⁴ The finite deformation anisotropic model is tested under monotonically increasing uniaxial tension loading illustrated in Figure 8. The material properties for both the matrix and

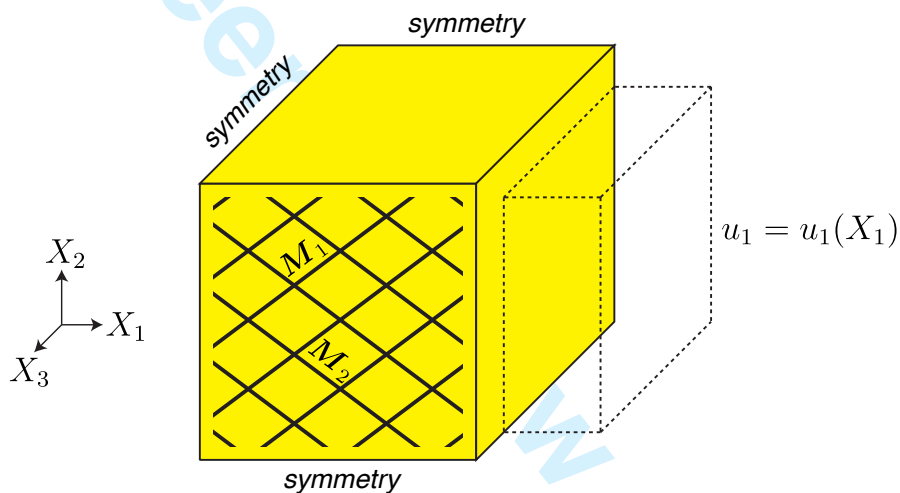


Figure 8: Schematic illustrating the uniaxial tension of a reinforced-fiber composite under finite deformations. Fibers are oriented along \mathbf{M}_1 and \mathbf{M}_2 .

⁴²⁵
⁴²⁶ microfibers are listed in Table 3.

⁴²⁷ The axial stress vs. stretch behavior of the uniaxial tension test is shown in Fig. 9(a),
⁴²⁸ where the X denotes the onset of material bifurcation. We use the two-step procedure
⁴²⁹ together with the adaptive time increment discussed in Sec. 4 for the detection of bifurcation.
⁴³⁰ Fig. 9(b) shows the degradation of the determinant function for all five parametrizations
⁴³¹ until material bifurcation is detected. In this loading test, all five parametrizations detect
⁴³² bifurcation at the same time, i.e., when the axial component of the deformation gradient
⁴³³ $F_{11} = 1.1798$.

⁴³⁴ As in the previous example, the computation time of the different parametrizations within
⁴³⁵ the loading increment leading to bifurcation is recorded and shown in Table 4. Again,
⁴³⁶ the density of the initial sampling is represented by the sampling interval and the number
⁴³⁷ of sampling points. In general, as the number of sampling points decreases, so does the

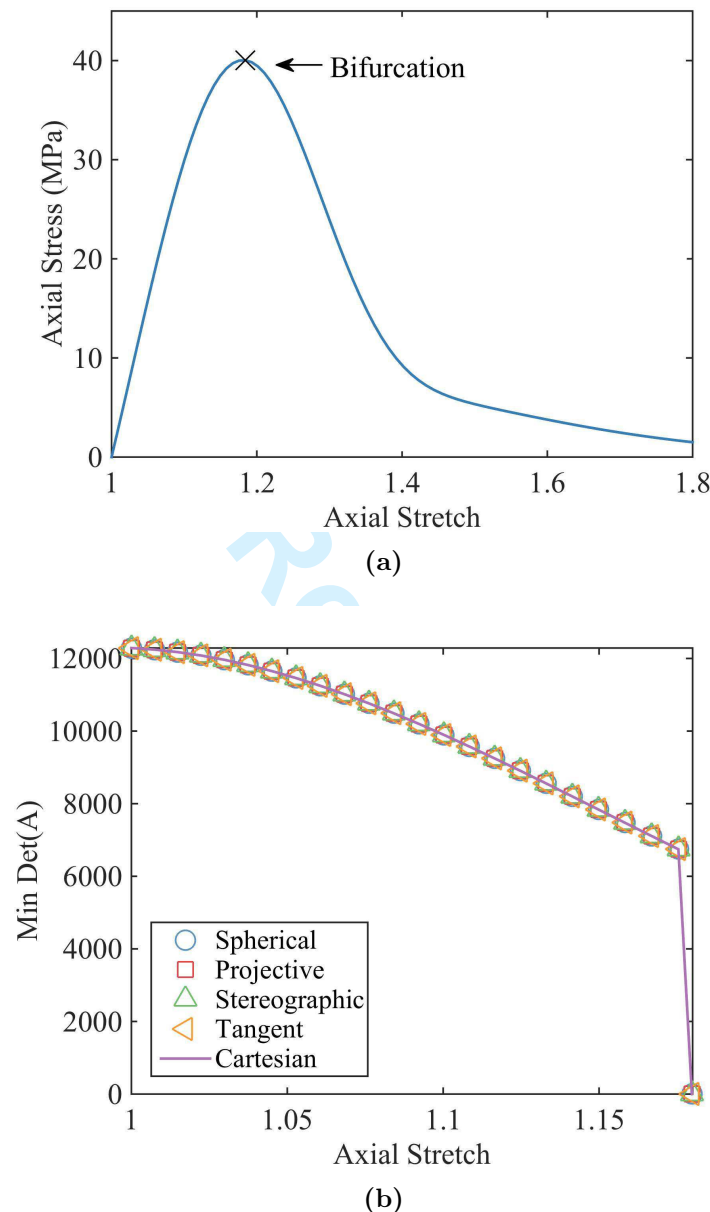


Figure 9: Uniaxial tension test on finite deformation anisotropic damage model: (a)stress vs. axial stretch, with the X indicating bifurcation, and (b) degradation of $\det \mathbf{A}$ for different parametrizations.

Matrix	Fibers
Lamé constant	$\lambda = 80$
Lamé constant	$\mu = 80$
Damage variable	$\xi_{\infty}^m = 1.0$
Damage variable	$\tau^m = 4.0$
Volume fraction	$f^m = 0.2$
	Elasticity constants
	$q_1 = q_2 = 1.0$
	$\xi_{\infty;1}^f = \xi_{\infty;2}^f = 1.0$
	$\tau_1^f = \tau_2^f = 4.0$
	Volume fraction
	$f_1^f = f_2^f = 0.4$
	Direction vector
	$\mathbf{M}_1 = (0.8, 0.6, 0.0)$
	$\mathbf{M}_2 = (0.8, 0.6, 0.0)$

Table 3: Material properties for anisotropic damage model

438 computation time. Fewer sampling points, however, may lead to a poor initial guess for
 439 the Newton iterative scheme, which may result in a greater overall computation time to
 440 arrive at a converged solution. Due to the added complexity of the material model, different
 441 parametrizations are more sensitive to the density of the initial sampling grids. The spherical
 442 parametrization fails to correctly detect the bifurcation when the sampling interval is greater
 443 than 0.6. The stereographic, projective and tangent parametrizations, though relatively more
 444 robust in this case, are computationally more expensive. The Cartesian parametrization is
 445 computationally efficient and at the same time, relatively insensitive to the sampling interval.

Interval	Points	Run Time (μs)				
		Spherical	Stereographic	Projective	Tangent	Cartesian
0.05	41	404	254	5828	330	412
0.1	21	224	207	926	212	214
0.2	11	192	181	296	187	122
0.3	7	174	210	250	187	132
0.4	5	217	208	268	189	111
0.5	5	176	—	239	—	123
0.6	3	171	173	228	215	281
0.7	3	208	175	193	157	141
0.8	3	—	213	187	183	101
0.9	3	—	214	225	204	99
1.0	3	—	—	225	—	118
1.5	1	—	—	—	—	—

Table 4: Computation time for different parametrizations in the uniaxial tension test within the loading increment leading to bifurcation. The dash “—” indicates that the parametrization fails to detect bifurcation in this loading increment.

446 To gain insights into the influence of the parametrizations on the determinant function

⁴⁴⁷ $\det \mathbf{A}$ as loading proceeds, we plot in Fig. 10 to Fig. 13 the landscapes at four different axial
⁴⁴⁸ stretch levels for different parametrizations. Moreover, the corresponding plane views of the
⁴⁴⁹ determinant landscapes at the bifurcation are also shown in Fig. 14, where the white stars
⁴⁵⁰ indicate global minima.

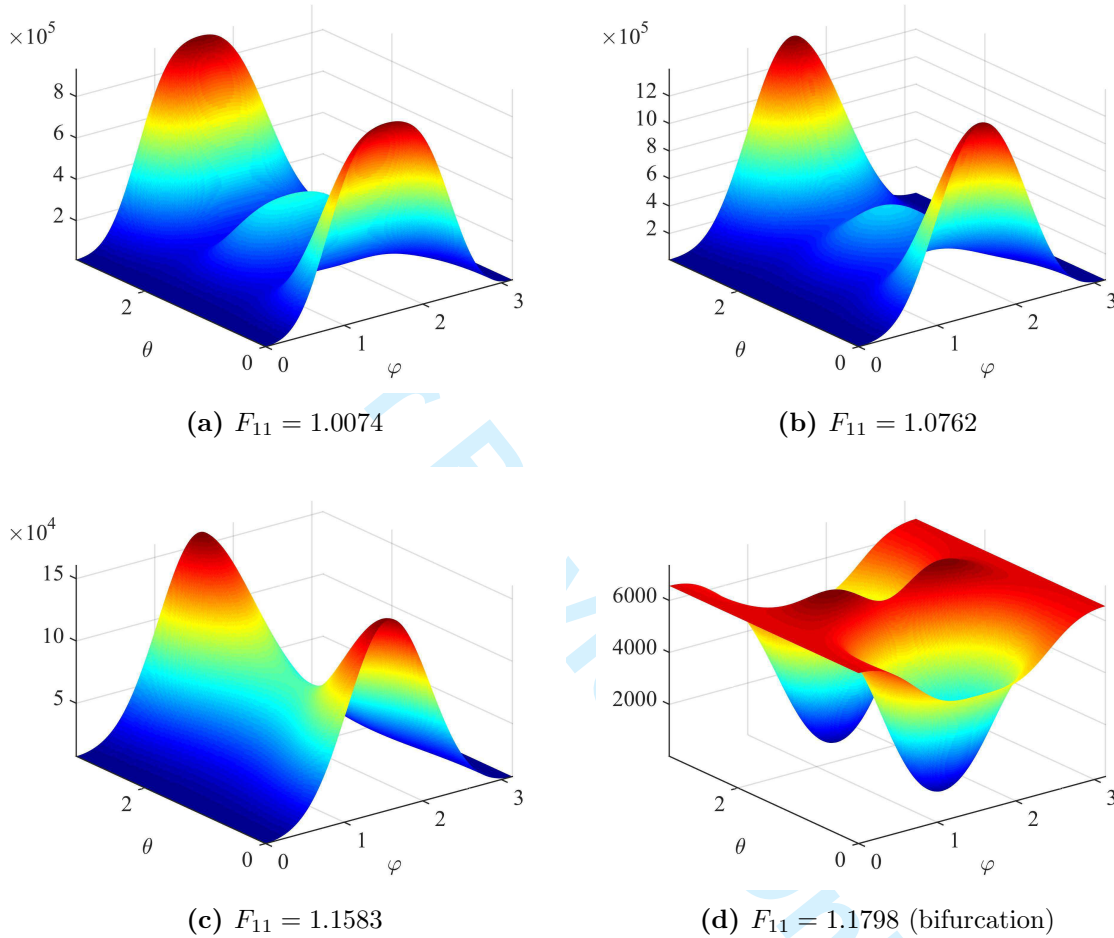


Figure 10: Spherical parametrization: landscapes of $\det \mathbf{A}$ for the uniaxial tension test of the finite deformation anisotropic model at different axial stretch levels.

⁴⁵¹ As can be seen from Fig. 13, the Cartesian parametrization again results in a simple, bowl-
⁴⁵² shaped landscape of the determinant function consistently throughout the loading process,
⁴⁵³ which is in contrast to the more complex landscapes of the spherical (Fig. 10), stereographic
⁴⁵⁴ (Fig. 11) and tangent (Fig. 12) parametrizations.

⁴⁵⁵ As in the case of the small deformation model example in Section 5.1, the robustness of the
⁴⁵⁶ different parametrizations on the detection of material bifurcation is analyzed by randomly
⁴⁵⁷ generating a single initial point for the Newton iterative scheme and eliminating the initial
⁴⁵⁸ sampling. A total of 1000 random initial guesses are generated for each parametrization. The
⁴⁵⁹ success rate and computation time are recorded and summarized in Table 5. The results are

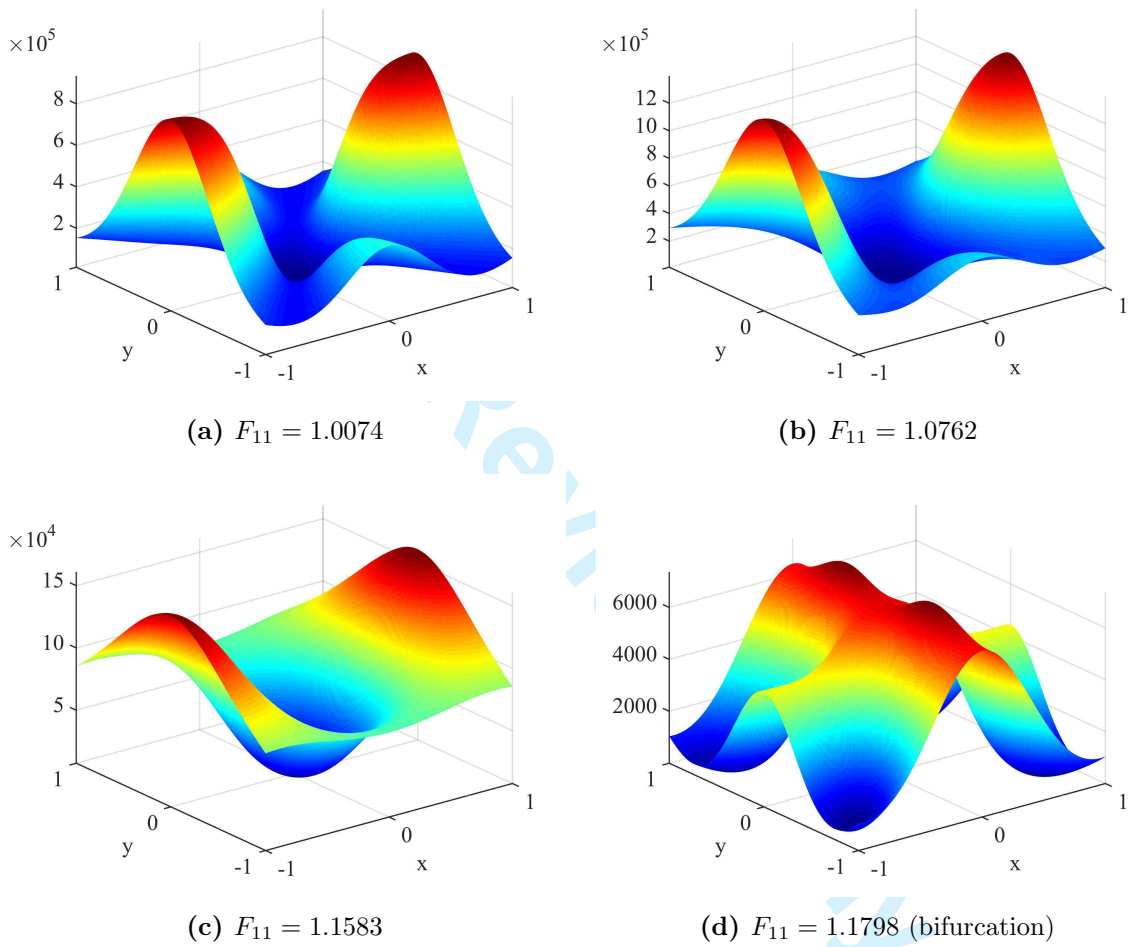


Figure 11: Stereographic parametrization: landscapes of $\det \mathbf{A}$ for the uniaxial tension test of the finite deformation anisotropic model at different axial stretch levels.

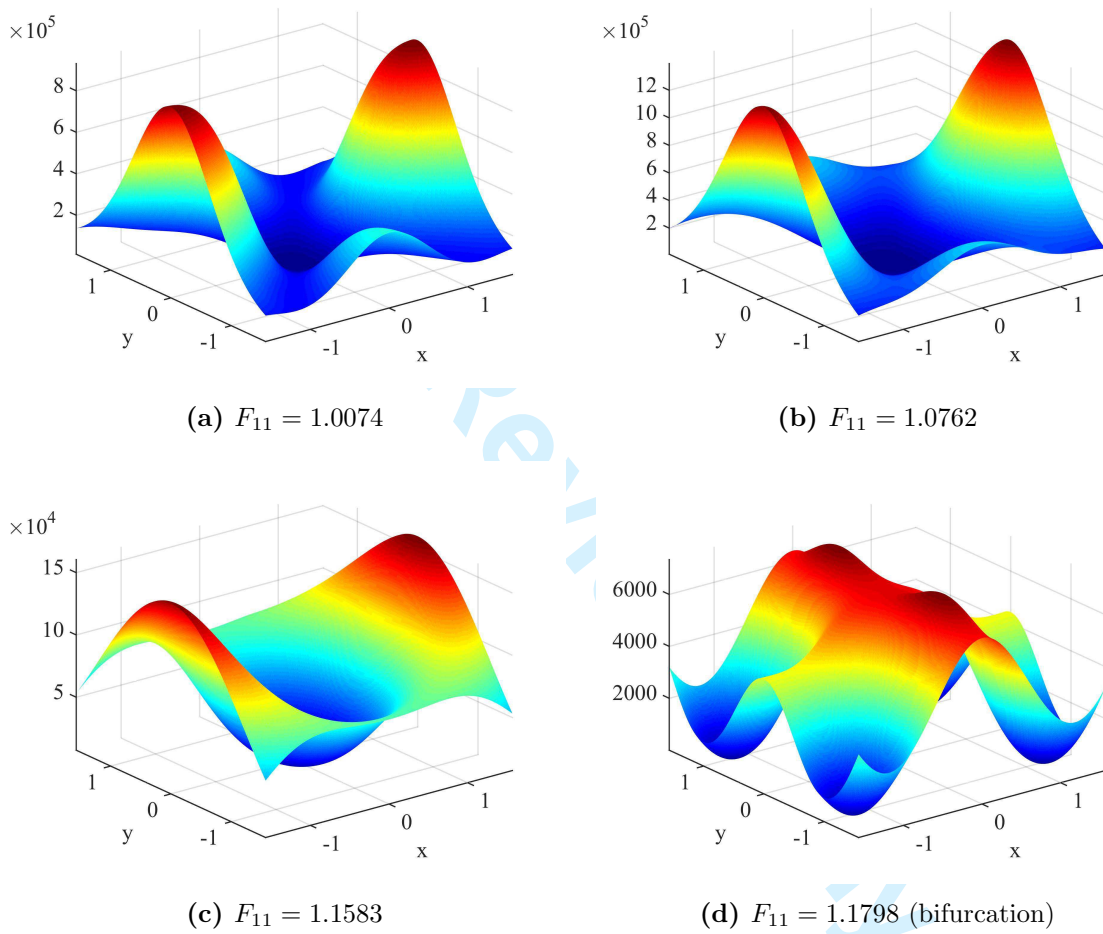


Figure 12: Tangent parametrization: landscapes of $\det \mathbf{A}$ for the uniaxial tension test of the finite deformation anisotropic model at different axial stretch levels.

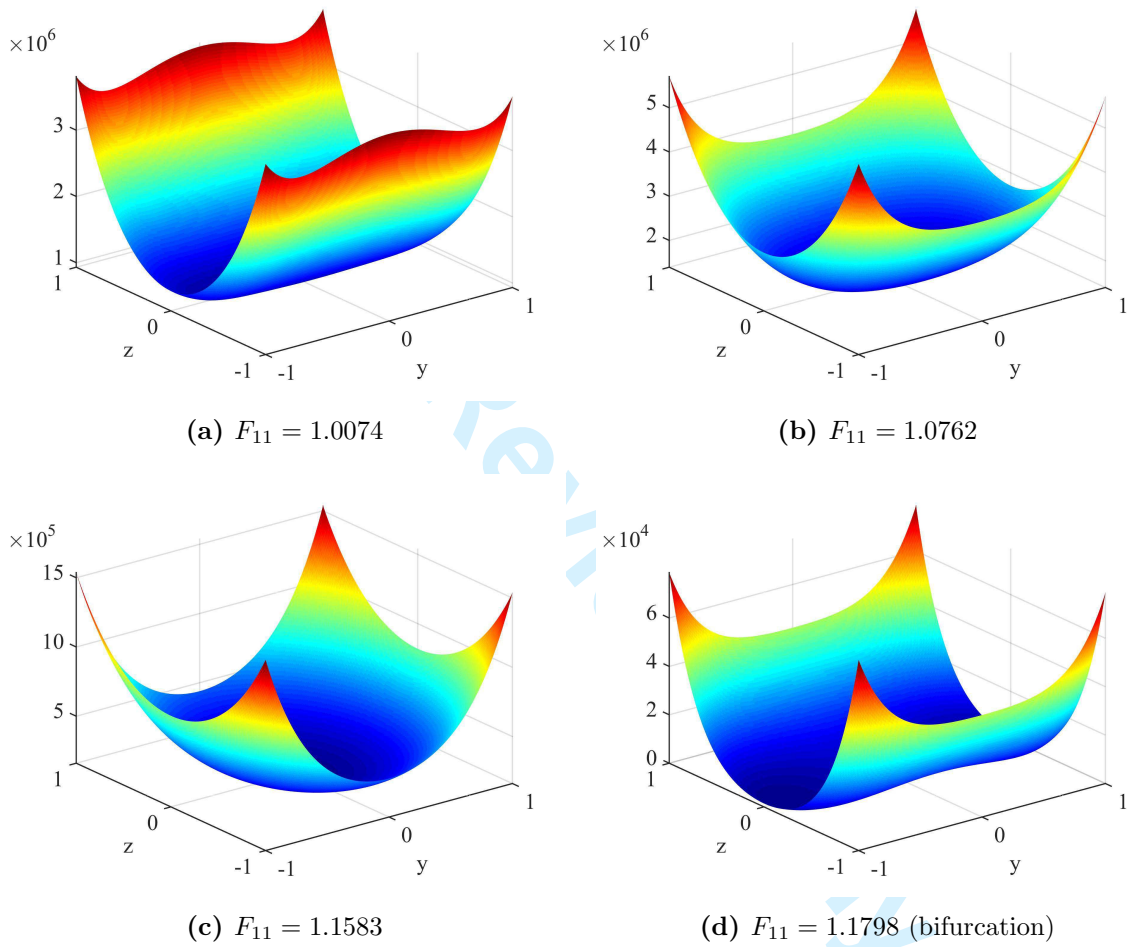


Figure 13: Cartesian parametrization: landscapes of $\det \mathbf{A}$ for the uniaxial tension test of the finite deformation anisotropic model at different axial stretch levels.

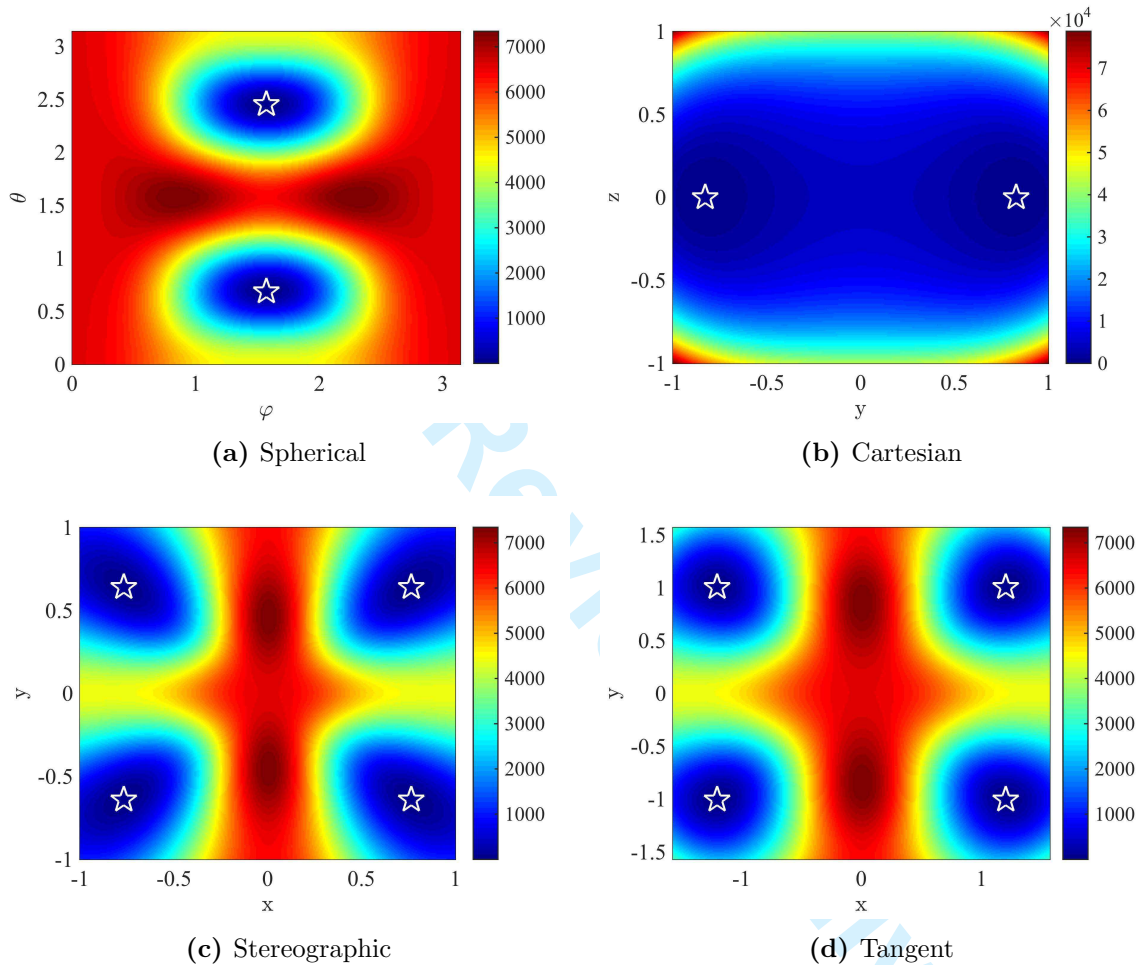


Figure 14: Plane views of the landscapes of the determinant of the acoustic tensor at bifurcation for the uniaxial tension on the finite deformation anisotropic model. The white stars indicate global minima at $\mathbf{n}_1 \approx (0.768, -0.641, 0.000)$ and $\mathbf{n}_2 \approx (0.768, 0.641, 0.000)$.

⁴⁶⁰ consistent with the small deformation model example, i.e., the Cartesian parametrization is
⁴⁶¹ the most robust and computationally efficient of all the ones tested.

	Spherical	Stereographic	Projective	Tangent	Cartesian
Success rate (%)	13.4	32.3	71.5	32.3	74.4
Average iteration count	4.37	4.91	8.04	4.57	6.93
Average run time (μ s)	270	274	483	245	267

Table 5: Anisotropic finite deformation model: success rate and computation time of the Newton iterative scheme with a single random initial guess. A total of 1000 random trials are performed for each parametrization.

⁴⁶² A visualization of the robustness of each parametrization with 1000 random initial guesses
⁴⁶³ is shown in Fig. 15. If the initial guess leads to a successful detection of bifurcation and its
⁴⁶⁴ directions, the point is marked as a solid circle (\bullet). Otherwise, it is marked as a cross (\times).

⁴⁶⁵ As in the case of the small deformation model example in Section 5.1, the Cartesian
⁴⁶⁶ parametrization performs better in terms of trade-off between computational efficiency and
⁴⁶⁷ robustness. In a non-linear large-scale finite element simulation, this optimal trade-off be-
⁴⁶⁸tween computational efficiency and robustness becomes critical. The Cartesian parametriza-
⁴⁶⁹tion thus provides a valuable tool in numerical bifurcation analysis.

⁴⁷⁰ 6 Conclusion

⁴⁷¹ In this work we examine the numerical performance of five different parametrizations for the
⁴⁷² detection of the loss of the ellipticity condition for the analysis of material instabilities. An
⁴⁷³ algorithm based on an initial sampling on a parametric grid followed by an iterative Newton
⁴⁷⁴ scheme is introduced as a robust and efficient method for the detection of the bifurcation
⁴⁷⁵ condition. In addition, we introduce a new parametrization that we term Cartesian for the
⁴⁷⁶ representation of the normal vector that defines the acoustic tensor in terms of the tangent
⁴⁷⁷ moduli tensor. We demonstrate with numerical examples that the Cartesian parametrization
⁴⁷⁸ offers the best performance in terms of computational efficiency and robustness as compared
⁴⁷⁹ with other four parametrizations. In summary, we find that:

- ⁴⁸⁰ 1. The classical bifurcation condition by means of the acoustic tensor can be used for
⁴⁸¹ a very general class of materials that include viscoelasticity, viscoplasticity and rate
⁴⁸² dependence by recourse to incremental variational constitutive updates.
- ⁴⁸³ 2. The parametrization of the normal vector significantly affects the complexity of the ob-
⁴⁸⁴ jective function to be minimized, which in turn influences the computational efficiency
⁴⁸⁵ and robustness of the algorithm used for the detection of bifurcation.

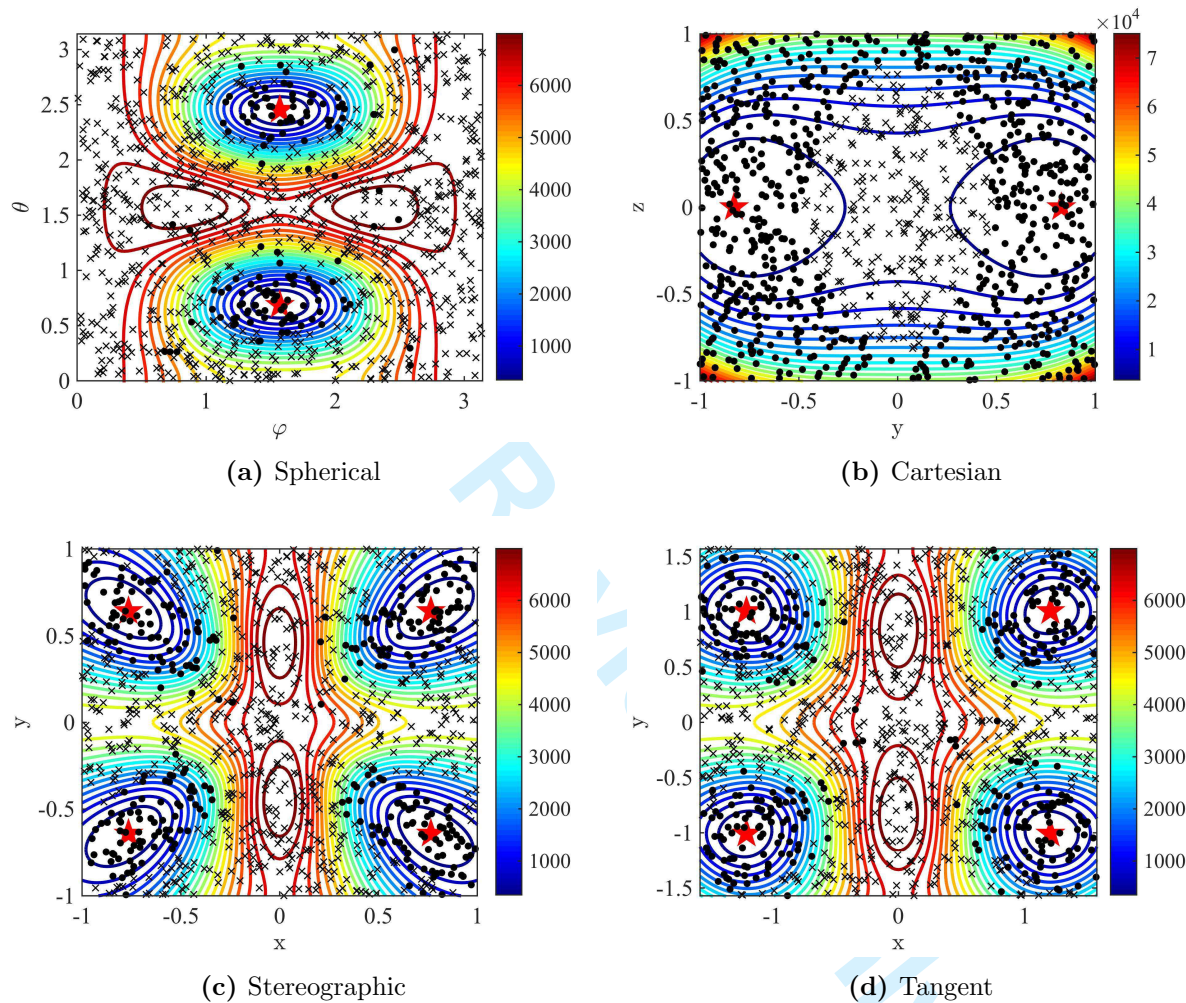


Figure 15: Anisotropic finite deformation model: results of the Newton iterative scheme with a single random initial guess plotted on contours of the determinant function at bifurcation. A solid circle (\bullet) indicates that the initial point leads to a successful detection of bifurcation and its directions. A cross (\times) indicates failure. A total of 1000 random trials are performed for each parametrization.

- 486 3. The commonly used spherical parametrization is efficient provided that the initial sam-
487 pling interval is fine enough and the initial guess is a good approximation to the mini-
488 mum. This parametrization, however, suffers from singularities for the representation
489 of points at its poles.
- 490 4. The stereographic and tangent parametrizations are the least robust, i.e., they are
491 more likely to have convergence issues. The projective parametrization is much more
492 expensive.
- 493 5. The Cartesian parametrization is the most robust for the material models and loading
494 conditions tested. It does not have any singularities and it is also computationally
495 efficient. The Cartesian parametrization represents an optimal trade-off between com-
496 putational efficiency and robustness and provides a valuable tool for efficient and robust
497 numerical analysis of material instability in large-scale finite element analysis.

498 References

- 499 [1] J.C. Simo, J. Oliver, and F. Armero. An analysis of strong discontinuities induced by
500 strain-softening in rate-independent inelastic solids. *Computational mechanics*, 12(5):
501 277–296, 1993.
- 502 [2] J. Oliver. Modelling strong discontinuities in solid mechanics via strain softening con-
503 stitutive equations. part 1: Fundamentals. *International journal for numerical methods
504 in engineering*, 39(21):3575–3600, 1996.
- 505 [3] J. Oliver. Modelling strong discontinuities in solid mechanics via strain softening con-
506 stitutive equations. part 2: Numerical simulation. *International journal for numerical
507 methods in engineering*, 39(21):3601–3623, 1996.
- 508 [4] F. Armero and K. Garikipati. An analysis of strong discontinuities in multiplicative finite
509 strain plasticity and their relation with the numerical simulation of strain localization in
510 solids. *International Journal of Solids and Structures*, 33(20-22):2863–2885, Aug 1996.
511 ISSN 0020-7683.
- 512 [5] N. Moës and T. Belytschko. Extended finite element method for cohesive crack growth.
513 *Engineering fracture mechanics*, 69(7):813–833, 2002.
- 514 [6] C.D. Foster, R.I. Borja, and R.A. Regueiro. Embedded strong discontinuity finite ele-
515 ments for fractured geomaterials with variable friction. *International Journal for Nu-
516 mercial Methods in Engineering*, 72(5):549–581, 2007.
- 517 [7] Q. Chen, J.E. Andrade, and E. Samaniego. AES for multiscale localization modeling
518 in granular media. *Computer Methods in Applied Mechanics and Engineering*, 200(33):
519 2473–2482, 2011.

- 520 [8] S. Antman. *Nonlinear Problems in Elasticity*. Springer, New York, second edition, 2005.
- 521 [9] R. Hill. Acceleration Waves in Solids. *Journal of the Mechanics and Physics of Solids*,
522 10(1):1–16, 1962. ISSN 0022-5096.
- 523 [10] M. Ortiz and L. Stainier. The variational formulation of viscoplastic constitutive up-
524 dates. *Computer Methods in Applied Mechanics and Engineering*, 171(3-4):419–444,
525 1999.
- 526 [11] M. Lambrecht, C. Miehe, and J. Dettmar. Energy relaxation of non-convex incremental
527 stress potentials in a strain-softening elastic-plastic bar. *International Journal of Solids
528 and Structures*, 40(6):1369–1391, Mar 2003. ISSN 0020-7683.
- 529 [12] C. Miehe, M. Lambrecht, and E. Gürses. Analysis of material instabilities in inelastic
530 solids by incremental energy minimization and relaxation methods: evolving deforma-
531 tion microstructures in finite plasticity. *Journal of the Mechanics and Physics of Solids*,
532 52(12):2725–2769, Dec 2004. ISSN 0022-5096.
- 533 [13] K. Weinberg, A. Mota, and M. Ortiz. A variational constitutive model for porous metal
534 plasticity. *Computational Mechanics*, 37:142–152, 2006.
- 535 [14] E. Fancello, J.P. Ponthot, and L. Stainier. A variational formulation of constitutive mod-
536 els and updates in non-linear finite viscoelasticity. *International Journal for Numerical
537 Methods in Engineering*, 65(11):1831–1864, Mar 12 2006. ISSN 0029-5981.
- 538 [15] J. Mosler and O.T. Bruhns. On the implementation of rate-independent standard dis-
539 sipative solids at finite strain - Variational constitutive updates. *Computer Methods in
540 Applied Mechanics and Engineering*, 199(9-12):417–429, 2010. ISSN 0045-7825.
- 541 [16] N. Bleier and J. Mosler. Efficient variational constitutive updates by means of a novel
542 parameterization of the flow rule. *International Journal for Numerical Methods in En-
543 gineering*, 89(9):1120–1143, Mar 2 2012. ISSN 0029-5981.
- 544 [17] J. Hadamard. *Leçons Sur La Propagation Des Ondes Et Les Équations De
545 L'hydrodynamique*. Hermann, Paris, 1903.
- 546 [18] T.Y. Thomas. *Plastic Flow and Fracture in Solids*. Academic Press, London, 1961.
- 547 [19] J.W. Rudnicki and J.R. Rice. Conditions for the localization of deformation in pressure-
548 sensitive dilatant materials. *Journal of the Mechanics and Physics of Solids*, 23(6):
549 371–394, 1975.
- 550 [20] J.R. Rice. The Localization of Plastic Deformation. In Koiter, W.T., editor, *Proceedings
551 of the 14th International Congress on Theoretical and Applied Mechanics*, volume 1,
552 pages 207–220, Amsterdam, 1976. North-Holland.

- 553 [21] H.L. Schreyer and M.K. Nielsen. Analytical and numerical tests for loss of material
554 stability. *International journal for numerical methods in engineering*, 39(10):1721–1736,
555 1996.
- 556 [22] R. Becker. Ring fragmentation predictions using the Gurson model with material sta-
557 bility conditions as failure criteria. *International Journal of Solids and Structures*, 39
558 (13-14):3555–3580, Jun-Jul 2002. ISSN 0020-7683. Symposium on Material Instabilities
559 and the Effect of Microstructure, UNIV TEXAS, AUSTIN, AUSTIN, TEXAS, MAY
560 07-11, 2001.
- 561 [23] J. Oliver and A.E. Huespe. Theoretical and computational issues in modelling material
562 failure in strong discontinuity scenarios. *Computer Methods in Applied Mechanics and*
563 *Engineering*, 193(27):2987–3014, 2004.
- 564 [24] L. Xue and T. Belytschko. Fast methods for determining instabilities of elastic-plastic
565 damage models through closed-form expressions. *International Journal for Numerical*
566 *Methods in Engineering*, 84(12):1490–1518, 2010.
- 567 [25] J. Oliver, A.E. Huespe, J.C. Cante, and G. Diaz. On the numerical resolution of the
568 discontinuous material bifurcation problem. *International journal for numerical methods*
569 *in engineering*, 83(6):786–804, 2010.
- 570 [26] M. Ortiz. An analytical study of the localized failure modes of concrete. *Mechanics of*
571 *Materials*, 6(2):159–174, 1987.
- 572 [27] M. Ortiz, Y. Leroy, and A. Needleman. A Finite-Element Method for Localized Failure
573 Analysis. *Computer Methods in Applied Mechanics and Engineering*, 61(2):189–214,
574 Mar 1987. ISSN 0045-7825.
- 575 [28] R Khen, T Désoyer, and A Dragon. Objective localization criterion and behavior for
576 finite deformation plasticity—a lagrangian formulation. *Archive of Applied Mechanics*,
577 68(2):85–102, 1998.
- 578 [29] D. Boussaa and N. Aravas. A numeric-symbolic approach to the problem of localization
579 of plastic flow. *Computational mechanics*, 27(4):324–331, 2001.
- 580 [30] J. Mosler. Numerical analyses of discontinuous material bifurcation: Strong and weak
581 discontinuities. *Computer Methods in Applied Mechanics and Engineering*, 194(9):979–
582 1000, 2005.
- 583 [31] C. Miehe, J. Schotte, and M. Lambrecht. Homogenization of inelastic solid materials at
584 finite strains based on incremental minimization principles. Application to the texture
585 analysis of polycrystals. *Journal of the Mechanics and Physics of Solids*, 50(10):2123–
586 2167, Oct 2002. ISSN 0022-5096.
- 587 [32] C. Truesdell and W. Noll. *The Non-Linear Field Theories of Mechanics*. Springer-
588 Verlag, 3rd edition, 2004. ISBN 0387550984.

- 589 [33] J.E. Andrade and R.I. Borja. Capturing strain localization in dense sands with random
590 density. *International Journal for Numerical Methods in Engineering*, 67(11):1531–1564,
591 Sep 10 2006. ISSN 0029-5981.
- 592 [34] M. Springmann, A. Kühhorn, M. Kuna, and M. Scherzer. Influence of strain localization
593 on parameter identification. *Journal of Engineering Materials and Technology*, 131(1):
594 011003, 2009.
- 595 [35] R.A. Regueiro and C.D. Foster. Bifurcation analysis for a rate-sensitive, non-associative,
596 three-invariant, isotropic/kinematic hardening cap plasticity model for geomaterials:
597 Part i. small strain. *International Journal for Numerical and Analytical Methods in
598 Geomechanics*, 35(2):201–225, 2011.
- 599 [36] J.C. Simo and D.D. Fox. On a Stress Resultant Geometrically Exact Shell-Model .1.
600 Formulation and Optimal Parametrization. *Computer Methods in Applied Mechanics
601 and Engineering*, 72(3):267–304, MAR 1989. ISSN 0045-7825.
- 602 [37] J. Gallier. *Geometric Methods and Applications: For Computer Science and Engineering*. Springer, June 2011. ISBN 9781441999603.
- 604 [38] G.A. Holzapfel. *Nonlinear solid mechanics*, volume 24. Wiley Chichester, 2000.
- 605 [39] Q. Chen, J.T. Ostien, and G. Hansen. Development of a used fuel cladding damage
606 model incorporating circumferential and radial hydride responses. *Journal of Nuclear
607 Materials*, 447(1):292–303, 2014.
- 608 [40] G.A. Holzapfel and R.W. Ogden. Constitutive modelling of arteries. In *Proceedings
609 of the Royal Society of London A: Mathematical, Physical and Engineering Sciences*,
610 volume 466, pages 1551–1597. The Royal Society, 2010.